SIZE MATTERS:
Impact Energy Absorption Across Five Decades of Length Scale

Jacob A. Rogers[a,*], Kailu Xaio[b], Paul T. Mead[a],
Charles U. Pittman, Jr.[c], Edwin L. Thomas[b], Justin W. Wilkerson[a], Thomas E. Lacy, Jr.[a,**]

[a] *J. Mike Walker '66 Department of Mechanical Engineering, Texas A&M University, College Station, Texas, 77843.*
[b] *Department of Material Science and Engineering, Texas A&M University, College Station, Texas, 77843.*
[c] *Department of Chemistry, Mississippi State University, Starkville, Mississippi, 39762.*

Abstract

The Laser-Induced Particle Impact Test (LIPIT) can be used to probe projectile, target, and synergistic projectile-target responses to high strain rate deformation at the microscale. LIPIT's advantages over other microscale launching techniques include the ability to controllably launch a single microparticle and precisely characterize the projectile momentum and kinetic energy before and after target impact. In addition, a LIPIT apparatus possesses a small laboratory footprint and is suitable for extension to high-throughput testing. Hence, LIPIT experiments have been used to study the dynamic response of many polymers, gels, and metals in different structural forms with various h_t/d_p ratios. These microscopic high-rate deformation behavior and impact energy absorption studies were used to suggest promising materials for macroscopic applications. Geometric scale, however, can significantly influence dynamic material behavior through scale-induced changes in event time, strain rate, projectile/target material homogeneity, and more. In this study, such geometric-scale effects are intentionally investigated. Noncrystalline alumina spheres ranging five orders of magnitude in diameter (d_p = 3 μm–10 mm) were launched into scaled h_t/d_p amorphous polycarbonate targets of thickness h_t at normal incidence using either LIPIT or a gas gun, depending on the scale. Projectile impact velocity and the projectile diameter to target thickness ratio were held constant in all experiments (v_i = 550 m/s and h_t/d_p = 0.25, respectively). Impact energies spanned from hundreds of joules down to nanojoules (eleven decades). The specific impact energy absorption (E_p^*), local plastic deformation, and deformation microstructure were compared across all scales. Length scale reduction sets in motion a remarkable 230% amplification in specific energy absorption and a 240% increase in relative impact deformation area. Corresponding numerical impact simulation results emphasize key limitations of current continuum-based

*Corresponding author. J. Mike Walker '66 Department of Mechanical Engineering, Texas A&M University, College Station, Texas, 77843, United States.
Email Address: jacob_rogers@tamu.edu
**Corresponding author. J. Mike Walker '66 Department of Mechanical Engineering, Texas A&M University, College Station, Texas, 77843, United States.
Email Address: telacyjr@tamu.edu

material models and indicate potential areas of improvement. These findings demonstrate that material property discoveries made using emerging high-throughput methods (LIPIT, nanoindentation, laser-driven flyers, *etc.*) may not be directly indicative of macroscopic behavior and performance.

Keywords: Laser induced particle impact test (LIPIT), Single-stage gas gun, Scanning electron microscopy (SEM), Optical microscopy, Specific energy absorption, Length scale, Strain rate, Polycarbonate, Alumina, Thin films, Profilometry, Laser confocal microscopy, Microspheres, Impact scaling, Geometric scaling, Elastic Plastic Impact Computation (EPIC) code

---

1. Introduction and Motivation

Nature's spectacular impacts include collisions of galaxies transcending eons [1, 2], asteroid-planetary impacts triggering mass extinctions [3], biological events like the potent strikes of mantis shrimp [4], and star-powering fusion of atoms lasting only zeptoseconds [5]. Similarly, human-engineered collisions play vital roles in asteroid/meteoroid redirection [6], construction and fabrication processes [7], hypersonic missile defense [8], kinetic energy weapon impacts [9], cold spray application [10], innovative drug delivery methods [11], and fusion power generation [12]. Investigations of impact dynamics and their outcomes fuel the development of ballistic armor [13], automobile collision passenger safeguards [14], and spacecraft micro-meteoroid/orbital debris shielding [15]. These impacts, driven by forces from gravity to atomic interactions, release energy ranging from yottajoules (10^{24} J) to attojoules (10^{-18} J) and can transform kinetic energy into thermal, chemical, potential, and mechanical energy, activating material elastic or inelastic deformation, fracture, fragmentation, melting, vaporization, sublimation, ionization, fission, and fusion. Amplifying this complexity, the mechanisms and processes at play can change dramatically with spatial and temporal scales.

Many impacts can be characterized by the projectile and target material properties, projectile diameter (d_p), target thickness (h_t), and impact velocity (v_i), provided that the target's lateral dimensions are large enough to render boundary effects negligible. The following discussion focuses on a set pair of projectile and target materials. For a given target thickness to projectile diameter ratio (h_t/d_p), increasing v_i shortens the primary event duration, which in turn raises the strain and heating rates. These rates are closely linked to the instantaneous material properties and phase [16]. Enlarging the spatial scale alone effectively lowers strain and heating rates through a corresponding increase in event duration. Decreasing this scale has the opposite effect. For a given combination of h_t, d_p, h_t/d_p, there exists a critical velocity at which target perforation will occur, commonly termed V_{50} [17]. Conversely, for a given combination of v_i, h_t, d_p, there is a critical geometric ratio, $(h_t/d_p)_{crit}$, that results in target perforation. When a rigid d_p projectile strikes a target at v_i, a ratio $h_t/d_p \ll (h_t/d_p)_{crit}$ typically yields thin film perforation, which resembles membrane stretching

and puncturing [18]. Elevating h_t/d_p to $(h_t/d_p)_{crit}$ alone causes a shift in impact behavior to ballistic limit perforation, characterized by target cratering, cracking, shear banding, spalling, bulging, petalling, and shear plugging [18, 19]. Semi-infinite penetration follows for $h_t/d_p \gg (h_t/d_p)_{crit}$, leading to extensive target penetration and cratering. Material hierarchical inhomogeneities, from macroscale aggregates to microscale grains and crystals, result in spatial variations in material properties and failure mechanisms that complicate matters further [20].

Historically, scaled impact research has predominantly focused on ballistic impact and planetary science, with attention given to composites, granular materials, and metals (see, *e.g.*, [21–25]). However, these studies often rely on certain simplifying assumptions (fully hydrodynamic behavior, axisymmetry, *etc.*) and are only applicable to a relatively narrow range of potential impact scenarios [*e.g.*, cratering with $h_t/d_p \gg (h_t/d_p)_{crit}$]. Despite the prevalence of natural and artificial impacts, the knowledge of how energy transformation processes and dissipation mechanisms vary with length scale remains insufficient, particularly when transitioning from macro ($\sim 10^{-2}$ m) to micro ($\sim 10^{-6}$ m) material length scales. Such a gap in understanding must be addressed as high-throughput material characterization techniques transition to increasing smaller length scales [26–28].

At the microscale, executing and characterizing controlled impacts is fraught with challenges in experimental repeatability, measurement uncertainties, sample preparation, and stochastic variations in material properties. The Laser-Induced Particle Impact Test (LIPIT) has become an attractive method for probing microscale projectile, target, and synergistic projectile-target responses to high strain rate deformation [29–34]. LIPIT's advantages over other microscale launching techniques include the ability to controllably launch a single microparticle with relatively low kinetic energy (∼nanojoules) and precisely characterize the projectile momentum and kinetic energy before and after target impact. A LIPIT apparatus also has a small laboratory footprint ($\sim 1 \times 1$ m^2) and is suitable to employ in high-throughput testing (Fig. 1a) [35]. LIPIT experiments have been applied to investigate impact responses of polymers, gels, and metals, in various structural forms [34–41]. These prior studies have leveraged *microscopic* high-rate deformation, failure, and relative impact energy absorption results to identify promising materials for *macroscopic* applications. However, the specific energy absorbed in these microscopic events often exceeds macroscopic counterparts by at least an order of magnitude. For reference, Fig. 1b displays a comparison between the specific energy absorption (E_p^*; more later) values obtained from microscopic and macroscopic experiments, as reported in a previous study [35]. Some microscopically determined E_p^* values [*e.g.*, for multi-walled carbon nanotube (MWCNT) sheets] exceed macroscopic values for metals by over 2,300%! This stark difference underscores the need to exercise extreme caution when extrapolating microscopic material behavior, particularly at high rates, without a comprehensive grasp of length scale effects.

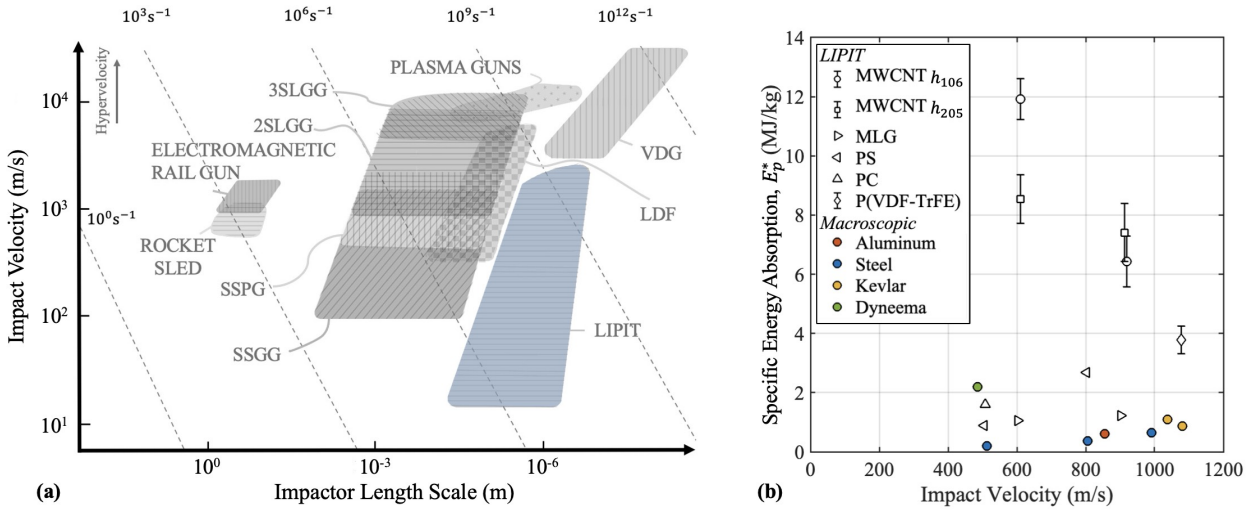

Figure 1: An overview of relevant launching techniques and experimental results from the literature: (a) representative launch capabilities as a function of impactor scale and (b) specific energy absorption as a function of impact velocity for macro- and micro-scales. Techniques include single-stage gas gun (SSGG), single-stage powder gun (SSPG), two-stage light gas gun (2SLGG), three-stage light gas gun (3SLGG), Van de Graaff accelerators (VDF), laser-driven flyers (LDF), laser-induced particle impact tests (LIPIT), rocket sleds, rail guns, and plasma guns. Materials impacted with similar h_t/d_p ratios include multi-walled carbon nanotubes (MWCNT) of thicknesses h_{106} and h_{205}, multi-layer graphene (MLG), polystyrene (PS), polycarbonate (PC), poly(vinylidene fluoride-co-trifluoroethylene) P(VDF-TrFE), aluminum, steel, Kevlar, and Dyneema. Figures were adapted from Refs. [35, 39].

Studying scale-induced changes in impact phenomena requires careful consideration of factors such as the projectile and target materials and geometries, as well as the impact velocity. The high sensitivity of polymer mechanical properties to temperature, pressure, and test rate, combined with the extreme conditions created in ballistic experiments, results in significant *gradients* in temperature, strain, strain rate, and stress state. These gradients evolve both over time and location. Consequently, the ballistic deformation of polymers stands out as the most scale-sensitive scenario (temporally and spatially). For instance, at the microscale, target thickness reduction alone has been shown to enhance E_p^* [42]. One systematic approach to isolating length scale influences involves the selection of macroscopically and microscopically homogeneous materials while holding the impact velocity and relative geometries of the projectile and target constant. Amorphous polycarbonate (PC) can be used to satisfy these criteria. PC is an important tough and transparent commercial thermoplastic with a broad range of applications in electronics, automobiles, construction, medicine, space exploration, and ballistic protection [43–49]. Moreover, PC inherently has just one material length scale—the root-mean-square distance between its chain ends.

For amorphous thermoplastic polymers such as PC, polystyrene (PS), and poly(methyl methacrylate) (PMMA), material yield stress is generally proportional to strain rate ($\dot{\varepsilon}$) and inversely proportional to temperature (T) [50]. These effects have been widely studied for glassy thermoplastics using various testing methods: universal tensile testing ($\dot{\varepsilon} \sim 10^{-4}$–$10^{1}$ s^{-1}), rheometry ($\dot{\varepsilon} \sim 10^{-3}$–$10^{3}$ s^{-1}), Split-Hopkinson

tension/compression/torsion bar testing ($\dot{\varepsilon} \sim 10^3$–$10^4$ s^{-1}), and Taylor impacts ($\dot{\varepsilon} \sim 10^5$ s^{-1}) [50–52]. Test temperatures have spanned $-150 \lessapprox T \lessapprox 200$°C. Across this range of loading rates and temperatures, the strength of glassy polymers can be attributed to their α and β transitions occurring at T_α and T_β, respectively [51]. For PC, $T_\alpha \approx 140$°C and $T_\beta \approx -100$°C. In its glassy range ($T_\beta < T < T_\alpha$), PC's tensile, compressive, and torsional yield stress all exhibit a linear increase with $\log \dot{\varepsilon}$ at constant T and a linear decrease with T at a constant $\dot{\varepsilon}$ (*i.e.*, PC behavior is described by the Eyring theory) [51, 52]. These relationships deviate from linearity at $T \approx -50$°C due to reduced backbone chain motion, leading to the observed β mechanical damping peak at T_β. Hydrostatic pressure increases the yield strength, bulk modulus, and T_g of PC. Post-yielding behavior in PC results from a balance between thermal softening and strain (and strain rate) hardening. At and above the yield stress, PC displays extensive viscous flow, while other glassy polymers, like PMMA and PS, undergo a ductile to brittle transition that is exacerbated by increasing strain rate [53]. PC maintains this ductility over a broad range of T and $\dot{\varepsilon}$ due to its unusually low T_β, contrasting with most thermoplastics that are brittle for $T < T_g$. PC, however, can embrittle when subjected to ultra-high strain rates, ultra-low temperatures, or annealing.

For $T < T_g$, PC generally yields, flows, converts approximately 50–60% of plastic work to heat, and exhibits damage localization in the form of shear banding and crazing [54–58]. For $T > T_g$, such damage localization is nonexistent. Fracture occurs as crazes nucleate and break down into tensile cracks, which propagate as new crazes form at their tips. These cracks eventually combine to form a fracture surface. Despite its low heat conductivity, PC's enhanced hardness through deformation-induced molecular orientation generally prevents its fracture from heat-induced shear instability. When subjected to macroscale ballistic impact ($\dot{\varepsilon} \lesssim 10^5$ s^{-1}), PC exhibits a variety of impact-driven failure modes, including dishing, petalling, cratering, cone cracking, and plugging [46]. The combined adiabatic heating from shocks and plastic work generates high temperatures, and this localized heating is enhanced by PC's low thermal conductivity. Elevated temperatures and ensuing visco-plastic flow during impact can potentially suppress or even "erase" evidence of shear banding, crazing, and other failure mechanisms. Even so, under macroscale hypervelocity impact conditions ($\dot{\varepsilon} \sim 10^6$–$10^7$ s^{-1}), PC appears to fail more brittly, hinting at a possible ductile-to-brittle transition with increasing strain rate [43]. Such a transition (if present) is influenced by projectile/target shapes, impact velocity, event duration, and more.

Although PC is extensively used and studied at the macroscale, it has been the subject of only one LIPIT study [49]. This previous work demonstrated that, for PC, increasing entanglement density (ν_e), either through higher molecular mass or reduced plasticizer content, noticeably increases E_p^*. PC, with its high entanglement density ($\nu_e \approx 10^{26}$ entanglements/m^3), stands out from other glassy polymers like PS ($\nu_e \approx 4 \times 10^{24}$). A higher entanglement density (more entanglement junctions per chain) generally enhances

material toughness and deformation resistance by forming an energy-absorbing network that restricts chain mobility, evenly distributes stress, enhances elasticity, and hinders crack growth [59–63]. Moreover, unlike other polymer glasses, PC's high-rate mechanical behavior is less susceptible to adiabatic heating, potentially explaining its 81% higher LIPIT E_p^* value at $v_i = 500$ m/s compared to PS (*cf.* Fig. 1b) [64]. Such material features could be responsible for the nominal entanglement-driven increases in E_p^* reported in [49]. This previous study, however, did not compare LIPIT results with corresponding macroscale tests. In fact, a systematic experimental analysis of how length scale influences ballistic impact phenomena from macroscale to microscale has yet to be conducted *for any material system*.

In this study, rigid noncrystalline alumina spheres ranging five orders of magnitude in diameter (d_p = 3 μm–10 mm) were launched into PC targets of thickness h_t at normal incidence using either LIPIT or a gas gun, depending on the scale. The projectile impact velocity ($v_i \approx 550$ m/s) and the ratio of projectile diameter to target thickness ($h_t/d_p \approx 0.25$) were held fixed for all experiments. Impact energies span from hundreds of joules down to nanojoules, significantly expanding on previous relevant investigations [49, 65, 66]. The specific impact energy absorption (E_p^*), local plastic deformation, and deformation microstructure are compared across all considered scales. The decrease in length scale results in a significant increase in specific energy absorption and relative deformation area. Numerical predictions of PC impact behavior are combined with the experimental results to show limitations in current continuum-based material modeling approaches. These preliminary observations show that length scale influences cannot be ignored when developing and employing emerging high-throughput experimental techniques that promise accelerated material discovery (*e.g.*, LIPIT, laser-driven flyers, and nanoindentation). Moreover, macroscopically observed impact phenomena and accompanying theory/models may not translate well to the microscale. In light of these implications, this study seeks to explore the influence of geometric scale on impact phenomena.

2. Methodology: Scaling the Impact

Thin films of PC were perforated at $v_i \approx 550$ m/s by noncrystalline rigid alumina spheres 3, 10, 100, 500, 1,000, 4,000, 10,000 μm in diameter. Regardless of length scale, the ratio of target thickness to projectile diameter (h_t/d_p) was fixed at roughly 0.25. These v_i and h_t/d_p values guaranteed target perforation while preserving the projectile's integrity. Maintaining v_i and h_t/d_p ensured comparable impact conditions, enabling a robust assessment of the role length scale plays in PC's deformation, failure, and specific energy absorption. The breadth of geometric scales probed in this study necessitated the use of two distinct projectile launching techniques. For the 3 μm and 10 μm diameter projectiles, a LIPIT apparatus in the Materials

Microstructures and Properties Laboratory at Texas A&M University (TAMU) was employed [40, 41].[1] The LIPIT technique involves using a laser pulse to ablate a gold film sandwiched between a glass substrate and a polydimethylsiloxane (PDMS) film [31, 35, 39, 42, 67]. Before launch, microparticles were distributed on the elastomer on the side of the "launch pad" that faces away from the laser's point of incidence (Fig. 2a). The launch pads were prepared as described in Ref. [41]. The laser pulse generates a plasma that expands and rapidly deforms the PDMS layer, propelling a projectile through lab air (∼101 kPa) at high velocity towards a target (Fig. 2b). The laser power can be adjusted to vary the projectile's launch velocity. In general, microparticles with diameters ranging 1–50 μm can be readily accelerated to velocities surpassing 1 km/s using this technique. A dedicated study to probe how length scale *and* velocity influence impact phenomena together is ongoing.

The remaining projectiles were launched using a single-stage gas gun (SSGG) and accompanying aerobal-listic range located within the TAMU Hypervelocity Impact Laboratory (HVIL) [68].[2] The SSGG launching mechanism operates using helium gas, initially contained in a high-pressure reservoir at pressures up to 34 MPa (Fig. 2c). Upon remote activation of a fast-acting valve, the He gas rapidly expands down the launch tube (barrel), accelerating a projectile towards its target (Fig. 2d). The SSGG can launch *single* projectiles ranging from 2.0–12.7 mm in diameter or *clusters* of particles down to 100 μm in diameter using a simultaneously launched distributed particle (SLDP) technique, to velocities ranging 0.1–1.5 km/s [69]. As an aside, launch velocities up to 8 km/s can be achieved using the HVIL two-stage light gas gun [68]. For the SSGG technique, a *single* projectile or *collections* of projectiles were loaded into a four-piece spherical cavity sabot. During free-flight through a tank containing lab air (∼101 kPa), the sabot segments radially separated from the projectile(s). The projectile(s) then passed through an annular steel plate, which halted the sabot. Single 4 mm and 10 mm spheres were launched in an appropriately sized sabot, while the SLDP technique was used to launch the 100, 500, and 1,000 μm diameter particles to increase the likelihood of observable target impact (increase experimental success). The lab air conditions used to separate the sabot segments also induced radial SLDP dispersion *via* aerodynamic forces. This launch process resulted in a well-distributed impact site pattern on the corresponding PC thin film, with individual sites being far enough apart to be considered as separate impacts (nearest neighbor impact site spacing $\gg 10 d_p$) [69].

The PC target materials were sourced from Plaskolite, LLC. [TUFFAK®; h_t: 1,016 μm ($PC1^{1016}$) and 2,380 μm ($PC1^{2380}$)] [70] and Rowland Advanced Polymer Films [RowTec®; h_t: 127 μm ($PC2^{127}$) and 254 μm ($PC2^{254}$)] [71]. Differential scanning calorimetry (DSC) curves for both PC1 and PC2 samples show

[1] Material Microstructures and Properties Laboratory Website: `https://elt.engr.tamu.edu/`.

[2] TAMU Hypervelocity Impact Laboratory Website: `https://telacyjr.engr.tamu.edu/facility/hypervelocity-impact-laboratory-hvil/`.

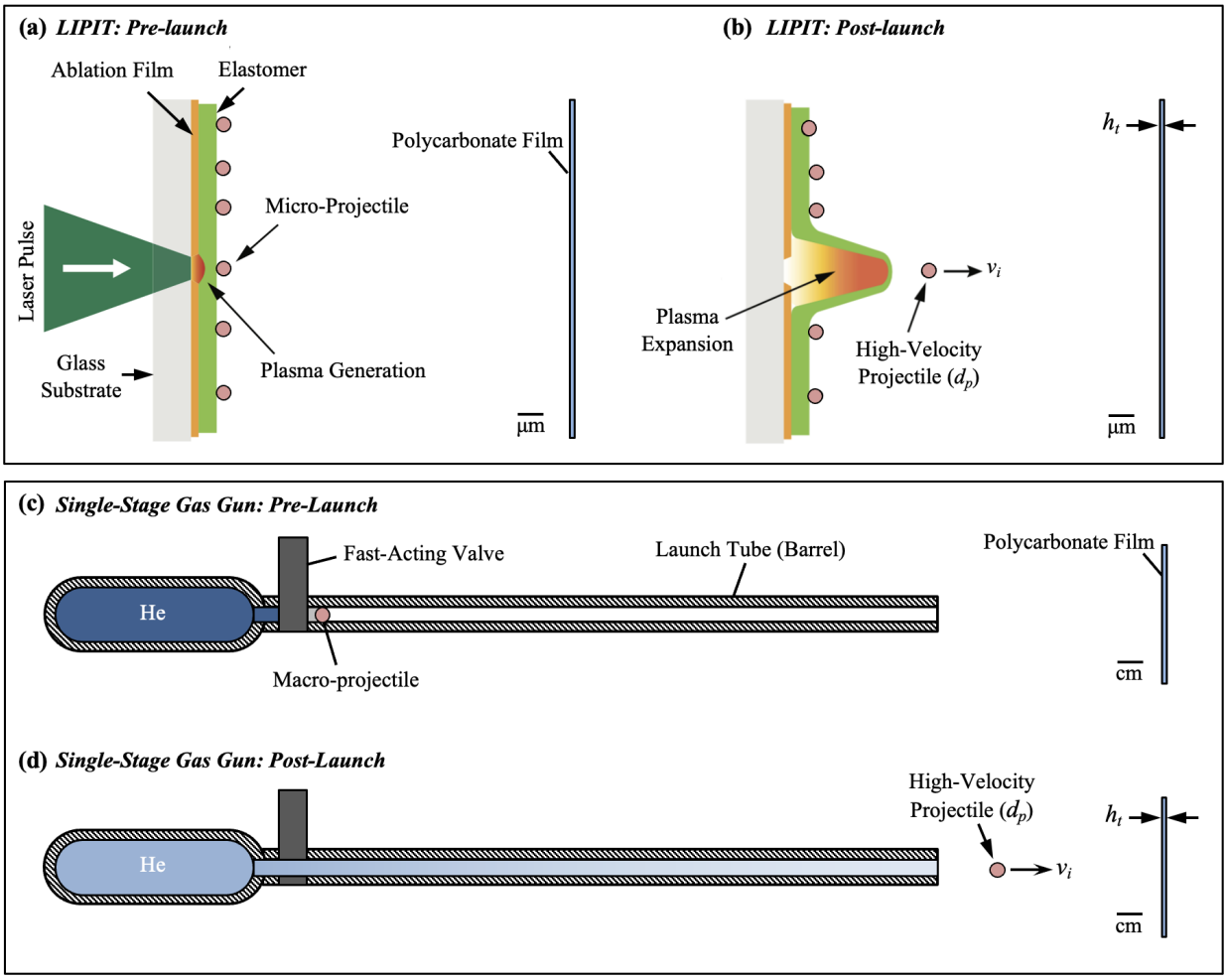

Figure 2: Projectile launching devices employed in this study: (a, b) a laser-induced particle impact test (LIPIT) apparatus and (c, d) a single-stage light gas gun. Both devices are shown in (a, c) pre- and (b, d) post-launch configurations. The LIPIT schematic was adapted from Ref. [35].

the materials have very similar glass transitions and glass transition temperatures (T_g = 148–153°C) (Fig. 3a). Both materials had a mass density of ρ_t = 1.20 g/cc and key mechanical properties that differed by less than 3% (see Supplementary Information, Sect. SI.3). The polymers' molecular weight averages (M_n: number average, M_w: weight average, M_z: Z-average) and molecular weight distribution ($PDI = M_w/M_n$: polydispersity) were measured using a TOSOH Ambient Temperature gel permeation chromatography (GPC) instrument with tetrahydrofuran (THF) as the solvent and polystyrene as the calibration standard. Both commercial materials had similar chromatographs: (PC1) $M_n = 27,737$ g/mol, $M_w = 55,711$ g/mol, $M_z = 87,908$ g/mol, $PDI = 2.01$ and (PC2) $M_n = 28,927$ g/mol, $M_w = 55,876$ g/mol, $M_z = 87,749$ g/mol, $PDI = 1.93$ (see Table S3 in Supplementary Information, Sect. SI.4).

The sample preparation technique was dependent on the film thickness. Targets with h_t = 127, 254, 1,016, and 2,380 μm were cut directly from the as-received PC1 or PC2 material and placed between two aper-

tured steel fixture plates (Fig. 3b and 3c). The 30 μm thick samples ($PC2^{30}$) were created by heated compression of the $PC2^{127}$ material. Given the small in-plane dimensions of the resulting targets (around 25.4 mm), a custom fixture with a grid pattern was created to hold multiple square thin films (Fig. 3d). This arrangement enhanced the likelihood of target impact during a given SLDP launch, thereby facilitating more extensive post-impact analysis. For LIPIT samples, the $PC2^{127}$ material was dissolved using 50/50 dichloromethane/toluene, then deposited on a silicon wafer attached to a spin coater. High-rate rotation and solvent evaporation yielded roughly 0.75 μm ($PC2^{0.75}$) and 2.25 μm ($PC2^{2.25}$) thick films, which were placed on a transmission electron microscopy (TEM) grids serving as LIPIT target fixtures (Fig. 3e). For all macroscopic SSGG experiments, the target assembly (target plus fixture) was centered on the launch tube (impact) axis. Translation stages were used as part of the LIPIT apparatus to identify a suitable projectile on the launch pad and impact site on the target inside a TEM grid square. In all experiments, target boundaries were far enough from the impact point to prevent in-plane reflected waves from affecting penetration/perforation dynamics (*i.e.*, perforation times were less than ∼10% of wave travel times; see Supplementary Information, Sect. SI.2).

Alumina (Al_2O_3) was chosen as the projectile material due to its relative homogeneity across the given length scales. The noncrystalline spheres were sourced from various commercial vendors depending on the diameter (d_p): Huake Scientific Research Materials Co., Ltd. (d_p = 3 μm and 10 μm), Corpuscular Microspheres-Nanospheres (d_p = 100 μm), Goodfellow Cambridge Ltd. (d_p = 500 μm and 1,000 μm), and Kyocera Corporation ($d_p = 4,000$ μm and 10,000 μm). For reference, Fig. 4 shows representative images of the projectiles at each length scale captured with either an optical camera (Figs. 4a and 4b) or Thermo Fisher Helios NanoLab 660 dual-focused ion beam-scanning electron beam microscope operating with an incident beam energy and working distance of 1 kV and 4 mm, respectively (Figs. 4c–4g). In this figure, the projectile diameter (d_p) decreases from left to right and top to bottom: (a) 10 mm, (b) 4 mm, (c) 1 mm, (d) 500 μm, (e) 100 μm, (f) 10 μm, and (g) 3 μm. The spheres displayed consistent sphericities and diameters even at the finest length scale, maintaining relative uniformity and comparability across the impact experiments. With a density of $\rho_p = 3.95$ g/cc, the projectiles varied in mass from $m_p = 5.6{\times}10^{-11}$ g (d_p = 3 μm) to m_p =$2.1{\times}10^{0}$ g (d_p = 10 mm). To underscore the extensive range of scale, the given mass values were used to calculate the projectile impact kinetic energy *via* $E_i = {}^1\!/_2\, m_p v_i^2$, assuming $v_i = 550$ m/s and neglecting rotational kinetic energy (Fig. 4h). The ballistic impacts presented in this work span *eleven orders of magnitude* in kinetic energy (10^{-9}–10^{2} J), representing the broadest range ever addressed in a single experimental impact study.

Prior to each experiment, the target thickness was measured using either a digital caliper ($h_t > 100$ μm)

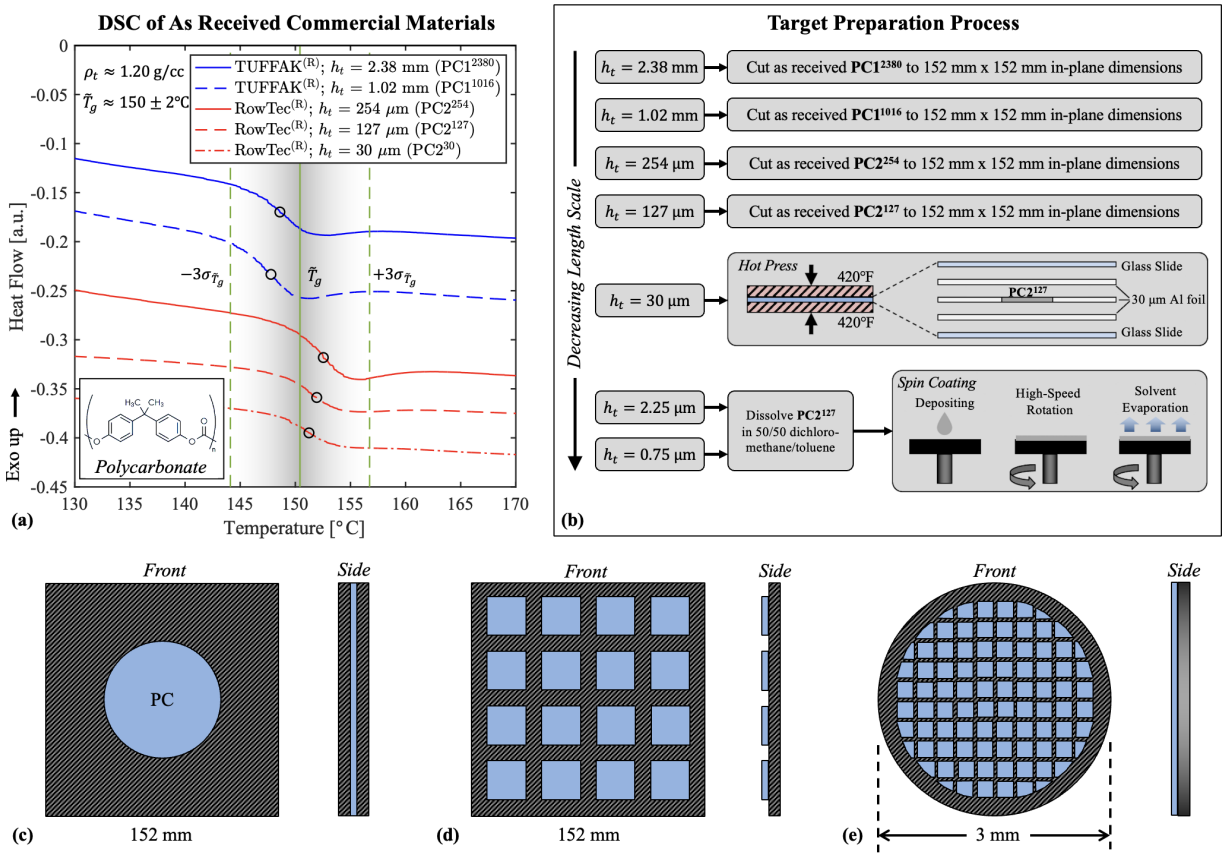

Figure 3: An overview of the polycarbonate (PC) targets: (a) a representative differential scanning calorimetry curve for each as-received target material and (b) the target preparation process for each film thickness, h_t. Two materials were used in target preparation: Plaskolite, LLC. TUFFAK® (PC1; $h_t = 1.02$, 2.38 mm) and Rowland Advanced Polymer Films RowTec® (PC2; $h_t = 0.75$, 2.25, 30, 127, 250 μm). All material had similar densities (ρ_t) and glass transition temperature (T_g) values. Targets were fixed (c) between apertured plates ($h_t = 127$, 254, 1,016, 2,380 μm), (d) in an array on a custom grid ($h_t = 30$ μm), or (e) on a 200 mesh TEM grid ($h_t = 0.75$, 2.25 μm).

or a Keyence VK-X3000 Three-Dimensional (3D) Surface Profiler laser confocal microscope ($h_t < 100$ μm).[3] In addition, the Keyence instrument was used to inspect the films for any obvious defects (impurities, second phase particles, cracks, *etc.*), significant thickness variations, and excessive surface roughness. Similarly, the diameter of each projectile was measured using either calipers, optical microscopy, or scanning electron microscopy (SEM), depending on the diameter. These steps were essential to ensure that the $h_t/d_p \approx 0.25$ ratio was largely maintained and that target inhomogeneities were minimized. During each experiment, high-speed cameras captured high-contrast, shadowgraphic images of the impact event. SSGG experiments employed a Shimadzu HPV-X2 camera, operating at a frame rate of 250 kHz and exposures ranging between 1000–1500 ns [72]. Light from high-intensity LED arrays, passed through a diffuser box, was used to illuminate the event [73]. A 50 mm lens was fitted onto the Shimadzu camera for the 1, 4, and 10 mm diameter

[3]Laser confocal and scanning electron microscopy were performed at the TAMU Small Scale Mechanical Behavior Laboratory.

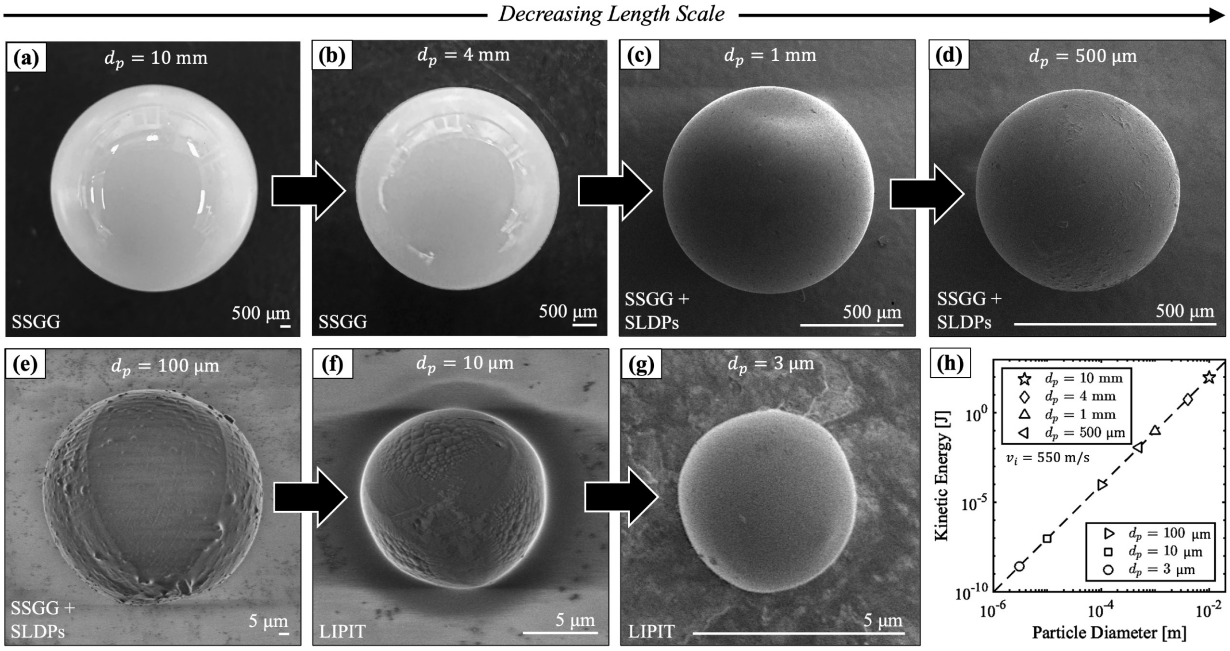

Figure 4: Micrographs showcase the alumina projectiles used in the impact experiments with the following diameters (d_p decreases from left to right): (a) 10 mm, (b) 4 mm, (c) 1 mm, (d) 500 µm, (e) 100 µm, (f) 10 µm, and (g) 3 µm. For reference of scale, the (h) impact kinetic energy ($E_i = {}^1\!/_2\, m_p v_i^2$) for each of these d_p values is plotted, assuming impact velocities of $v_i = 550$ m/s and projectile masses of $m_p = {}^1\!/_6\, \pi d_p^2 \rho_p$, where $\rho_p = 3.95$ g/cc is the projectile density.

particle impact experiments, while an Infinity K2 Distamax long distance microscope with a CF2 objective was used for the other tests. The LIPIT experiments were captured at a rate of 1 GHz and exposure of 5 ns using a Specialized Imaging SIMX camera [74]. A collimated laser served as the source of illumination for these tests. High-speed images of each projectile, taken just before impact, were analyzed alongside OM and SEM micrographs to verify its diameter. These diagnostic setups ensured consistent, comparable, and high-contrast shadowgraphic images across all scales [40, 68]. Figure 5 showcases annotated schematics of the projectile, target, launch technique, and the diagnostic tools, sequentially arranged in descending order from left to right. This simple, high-level representation of the scaled experiments highlights their uniformity in impact scenarios/conditions and diagnostic setups.

The impact conditions and relative projectile/target material properties ensured negligible *projectile* deformation and no projectile fragmentation occurred for all experiments. Each alumina projectile impacted its corresponding PC target with velocity v_i, remained intact during target perforation, and excited with a residual velocity v_r (Fig. 6a and 6b). Hence, the *in-situ* images also facilitated the measurement of v_i and v_r using open-source motion tracking softwares, such as Tracker [75] and ImageJ [76]. These velocity measurements were then used to compute the energy absorption of the target material, given by

$$E_p = \frac{1}{2} m_p v_i^2 - \frac{1}{2} m_p v_r^2 - E_{drag}, \tag{1}$$

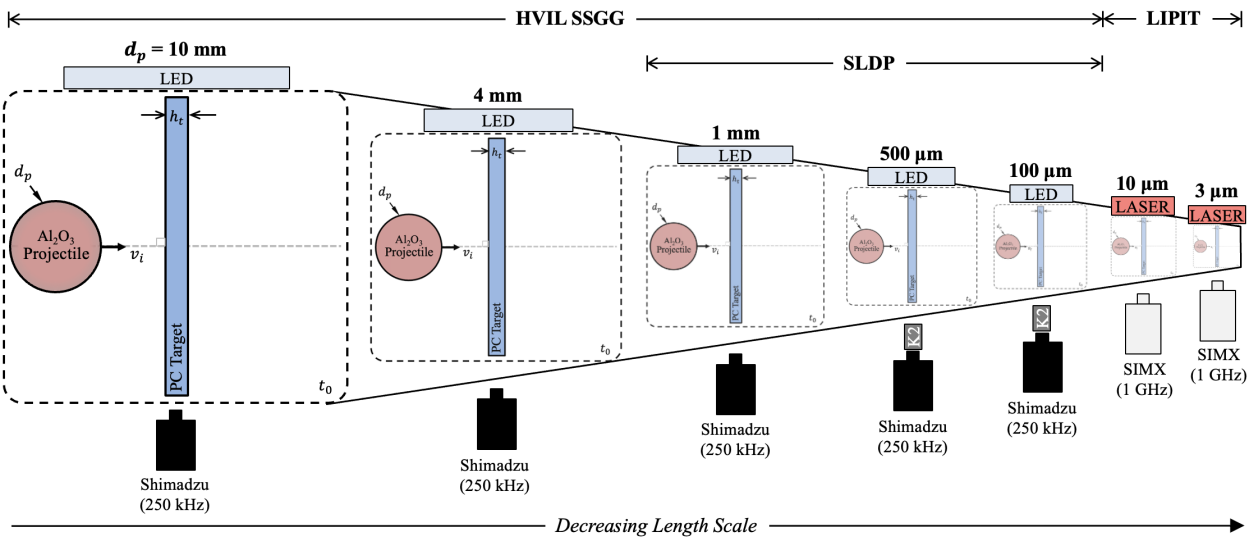

Figure 5: Schematic overview of the experimental methodology showcasing consistent diagnostics and impact scenarios across all scales, with the projectile diameter (d_p) provided in bold to highlight the scale. The projectile launch apparatus/technique (SSGG, SSGG + SLDP, or LIPIT) is also shown for reference.

where m_p is the mass of the projectile and E_{drag} is projectile kinetic energy loss due to drag, which was nonnegligible for the microsphere impacts and calculated using methods described in the supporting information of Refs. [42, 77]. The energy absorption can be normalized by the mass of an ideal plug of target material "ejected" by the projectile during target perforation (Fig. 6c) [39, 41, 49]. This nominal *specific energy absorption* facilitates ballistic performance comparisons across various materials and geometric scales and is given by

$$E_p^* = \frac{E_p}{\rho_t A_t h_t}, \tag{2}$$

where $\rho_t = 1.20$ g/cc is the mass density of the PC target material, $A_t = \pi/4\, d_p^2$ is the projected area of the projectile, and h_t is the thickness of the target. These calculations were instrumental in assessing a given target's impact energy dissipation in a way that was comparable across length scales and to relevant E_p^* values reported in the literature (see, *e.g.*, [49]).

After each experiment, optical micrographs of the perforations and out-of-plane deformation on both the impact and exit sides of the target were captured using a Keyence VK-X3000 3D Surface Profiler. The effective deformation diameter (D) of an in-plane circular region containing permanent deformation was calculated as twice the in-plane radius (R) from the center of impact to the radial location of ~5% vertical (z) target *impact* surface deflection, *i.e.*

$$R = r : \frac{|z_t - z_p(r)|}{z_t} \approx 5\%, \tag{3}$$

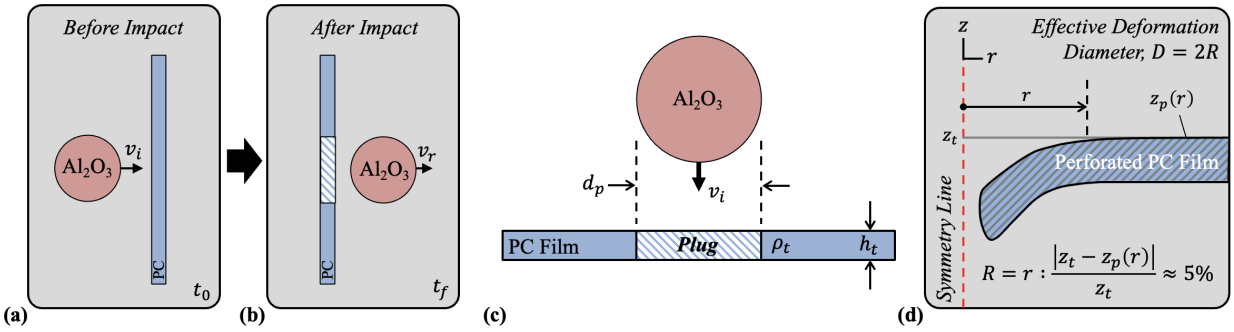

Figure 6: Simplified diagrams illustrate the projectile: (a) approaching the target at time t_0 with velocity v_i and (b) after perforating the target at time t_f with a residual velocity v_r. Diagram (c) represents the method for normalizing the energy absorption of the target, E_p, using the mass of a conceptualized "ejected" material plug (highlighted with crosshatching); the plug mass is defined as $m_t = \pi/4\, \rho_t h_t d_p^2$. The final diagram, (d), depicts the normalized deformation area concept, expressed as $A_d/A_p = D^2/d_p^2$, where D is the diameter of the circle defined by A_d.

where z_t is the constant vertical height of the undeformed target impact surface, $z_p(r)$ is the height of the deformed target impact surface, and r is the radial coordinate (Fig. 6d). This diameter was used to characterize the *normalized deformation area*,

$$\frac{A_d}{A_p} = \frac{D^2}{d_p^2}, \tag{4}$$

consistent with definitions used throughout the literature [49]. One-dimensional (1D) deformation profiles collected at each scale were normalized by the projectile diameter allowing for direct comparisons of the relative deformation for each test. SEM imaging of the LIPIT perforations on both the target impact and exit surfaces using the ThermoFisher Helios NanoLab 660 dual-focused ion beam-scanning electron beam microscope used for inspecting the alumina spheres (1 kV operating voltage, 4 mm working distance). Hence, the variations in deformation behavior and failure mechanisms across length scales were quantified. An overview of the experimental workflow is summarized in Fig. 7.

3. Results and Discussion for the Scaled h_t/d_p Impacts

This section highlights essential findings from the scaled impact experiments, including specific energy absorption (E_p^*) and normalized deformation area (A_d/A_p) measurements, as well as representative optical microscopy images and profilometry scans of each perforation on both the front and back surfaces of each target. SEM micrographs of the LIPIT perforations are also presented. E_p^* and A_d/A_p are also compared to calculated values from the Elastic Plastic Impact Computation code (EPIC) simulations across all considered length scales (see Supplementary Information, Sect. SI.6).

The constant h_t/d_p impact experiments were performed at seven distinct length scales, which can be described by the diameter of the alumina projectiles: d_p = 3, 10, 100, 500, 1,000, 4,000, and 10,000 μm.

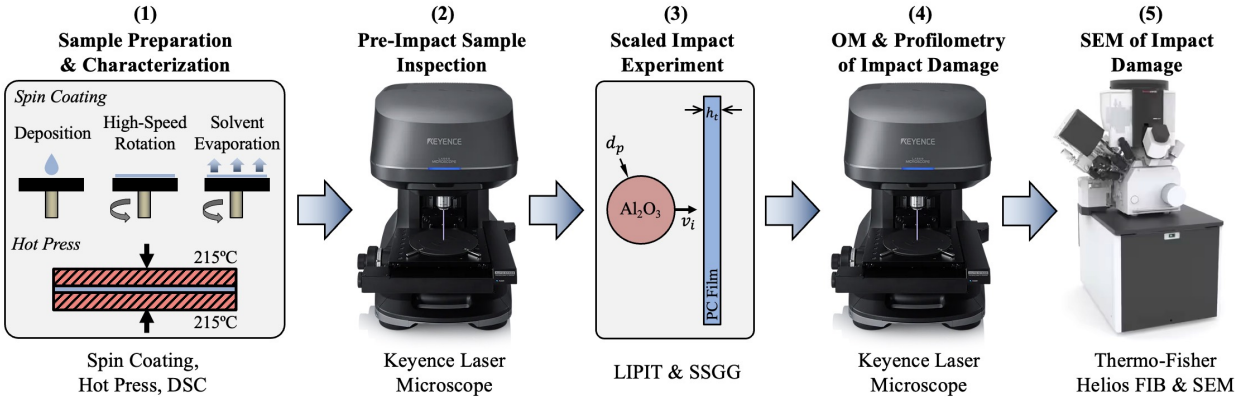

Figure 7: A summary of the experimental workflow employed in this study. Key steps include (1) sample preparation, (2) pre-impact sample inspection with the Keyence VK-X3000 3D Surface Profiler, (3) scaled impact experiment using either the LIPIT apparatus or SSGG, (4) optical microscopy and laser confocal microscopy of impact damage with the Keyence instrument, and (5) scanning electron microscopy (SEM) of impact damage using the ThermoFisher Helios NanoLab 660 dual-focused ion beam-scanning electron beam microscope.

For each scale, at least three tests were run to establish average data points and corresponding standard deviations, which tended to increase at smaller scales. LIPIT thin films targets varied slightly in thickness due to inherent variability in the spin coating process, affecting the h_t/d_p ratios. However, they remained near the intended value of 0.25. Similarly, thickness discrepancies in samples around $h_t = 30$ μm, made *via* compression molding, altered the h_t/d_p ratio. Regardless of length scale and launch technique (SSGG, SSGG + SLDP, or LIPIT), the projectile's motion was captured using high-speed shadowgraphy. Figure 8 shows in descending order representative high-speed images captured before (Figs. 8a, 8c, 8e, 8g, 8i, 8k, 8m) and after (Figs. 8b, 8d, 8f, 8h, 8j, 8l, 8n) each scaled impact event by either the HPV-X2 (d_p = 100, 500, 1,000, 4,000, 10,000 μm) or SIMX (d_p = 3 and 10 μm) camera. Yellow arrows and red dashed lines superimposed on the images highlight the direction of projectile motion and relative target thickness inside/on the corresponding fixture, respectively. The projectile impact velocity (v_i) and residual velocity (v_r) were determined for all experiments by tracking its horizontal motion across multiple shadowgraphs. The launching technique, relative length scale, and average impact and residual velocities are also shown in Fig. 8 for reference. Variations in v_i at a given length scale were relatively minor (<10%). The key experimental parameters (d_p, v_i, v_r, h_t, h_t/d_p, E_p^*, and A_d/A_p), as well as the launch apparatus used at each length scale, are summarized in descending order in Table 1.

The specific energy absorption [E_p^*, Eq. (2)] of each scaled PC target was calculated for all experiments using the measured v_i and v_r values provided in Table 1. The variations in experimental h_t and v_i values, coupled with measureable deviations in d_p, likely explain the standard deviations in E_p^* and A_d/A_p at a given scale, particularly the notable increase in standard deviations with decreasing d_p. A heightened sensitivity of the target material to velocity changes occurs as h_t decreases due to increasing strain and heating

rates (more later). This could also partially explain the observed higher standard deviations. Under the assumption of constant projectile-target homogeneous materials, relative geometries, and impact conditions, E_p^* would be expected to remain constant *in the absence of any scaling effects*. Contrarily, E_p^* exhibited a dramatic increase with a decrease in scale, ranging from approximately 0.4 MJ/kg for the $h_t = 2.38$ mm (thickest) target to as high as 1.5 MJ/kg for the $h_t = 0.75$ μm (thinnest) target (a roughly 230% increase; *cf.* Table 1). The specific energy absorption is plotted in Fig. 9a for each geometric scale, demonstrating an inverse power law relationship with projectile diameter ($E_p^* \propto d_p^{-0.16}$). The error bars on each data point represent the standard deviation in E_p^* provided in Table 1. The LIPIT E_p^* measurements align well with previously reported values for $v_i \approx 500$ m/s PC film impacts, though with reduced $h_t/d_p \approx 0.04$ ratios and $26{,}000 < M_w < 59{,}000$ g/mol [49]. The notable rise in E_p^* with decreasing scale shown in Fig. 9a emphasizes that without proper physical understanding and scaling laws, microscopic impact phenomena cannot be directly extended to the macroscale or *visa versa*.

Post-impact characterization and measurements often help unravel *in-situ* material behavior and failure. The effective deformation area (A_d; *cf.* Fig. 6d) provides a simple estimation of the extent to which the target material was engaged and subsequently affected (through permanent deformation or failure) by the impact event. To establish a comparison baseline that spans various length scales, this area was normalized by the projected area of the projectile [A_d/A_p; Eq. (4)]. Assuming no scaling effects, the normalized deformation area would remain largely unchanged. Interestingly, however, measurements taken from optical microscopy and laser confocal micrographs indicate a similar trend between the A_d/A_p and E_p^*, both increasing dramatically with decreasing length scale. In fact, the normalized deformation area rises by a factor of three from the largest ($d_p = 10$ mm, $h_t = 2.38$ mm) to the smallest ($d_p = 3$ μm, $h_t = 0.75$ μm) scale (Table 1). Similar to E_p^*, the LIPIT A_d/A_p values are consistent with the results of Chan *et al.* [49], who found that at the microscale, PC's E_p^* rises with entanglement density and deformation area. As shown in Fig. 9b, A_d/A_p follows a power law trend with projectile diameter ($A_d/A_p \propto d_p^{-0.16}$). Notably, the scaling

Table 1: A summary of the scaled impact experiments performed in this study. A minimum of three experiments were performed at each length scale to quantify the effects of impact velocity and target thickness variations on specific energy absorption (E_p^*).

No.	d_p (μm)	v_i (m/s)	v_r (m/s)	h_t (μm)	h_t/d_p	Launch Apparatus	E_p^* (MJ/kg)	A_d/A_p
1	10,000±2.5	561±29	482±29	2,380±130	0.24±0.01	SSGG	0.38±0.02	1.43±0.00
2	4,000±2.5	537±20	437±20	1,016±25	0.25±0.01	SSGG	0.42±0.02	1.70±0.00
3	1,000±2.5	539±4	434±4	254±25	0.25±0.03	SSGG SLDP	0.45±0.01	1.82±0.01
4	500±2.5	529±4	385±4	127±13	0.25±0.03	SSGG SLDP	0.57±0.01	2.15±0.02
5	100±2.5	523±47	251±47	30±5	0.30±0.05	SSGG SLDP	0.77±0.16	2.66±0.13
6	10±0.80	522±42	207±42	2.25±0.25	0.23±0.04	LIPIT	1.12±0.15	3.92±0.62
7	3±0.32	535±34	38±34	0.75±0.05	0.25±0.04	LIPIT	1.25±0.24	4.81±1.01

d_p, projectile diameter; v_i, projectile impact velocity; v_r, residual velocity; h_t, target thickness; h_t/d_p, target-thickness-projectile-diameter ratio; E_p^*, specific energy absorption [Eq. (2)]; A_d/A_p, normalized deformation area [Eq. (4)].

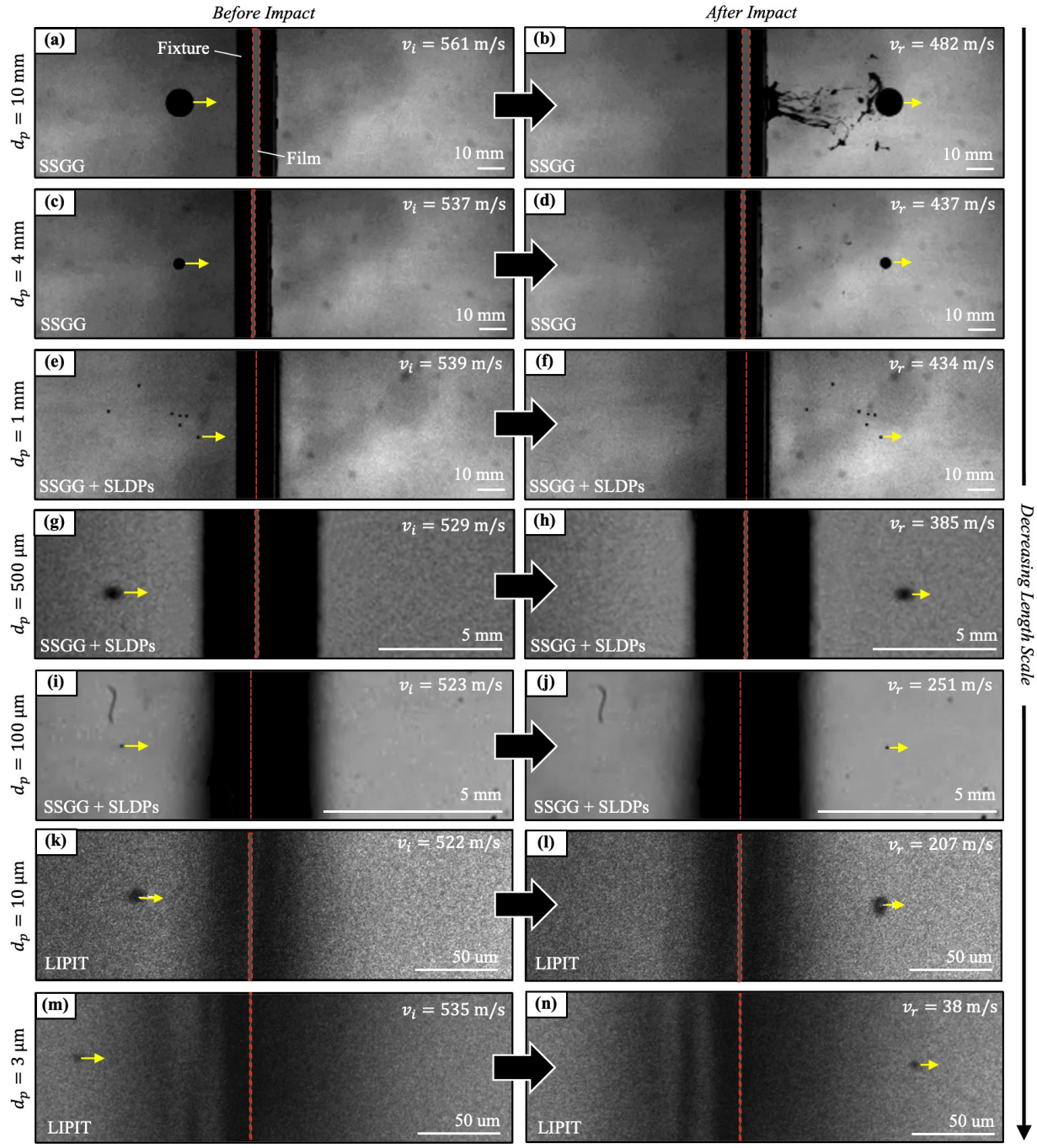

Figure 8: High-speed images capture the impact events: the alumina projectiles in images (a, c, e, g, i, k, m) are depicted prior to impact, and those in images (b, d, f, h, j, l, n) are shown after target perforation. Each row in the image array corresponds to a specific projectile diameter (d_p), which decreases sequentially from the top to the bottom. The target films are highlighted using red dotted lines for enhanced visibility (the dark areas around the films indicate target fixtures). Yellow arrows show the direction of projectile motion. Information provided alongside each series details the launching method (SSGG, SSGG + SLDP, or LIPIT), the impact velocity (v_i), residual velocity (v_r), and an accompanying scale.

exponents for A_d/A_p and E_p^* are virtually the same. This trend in A_d/A_p indicates that as the length scale decreases, a larger proportion of the target material undergoes deformation and failure.

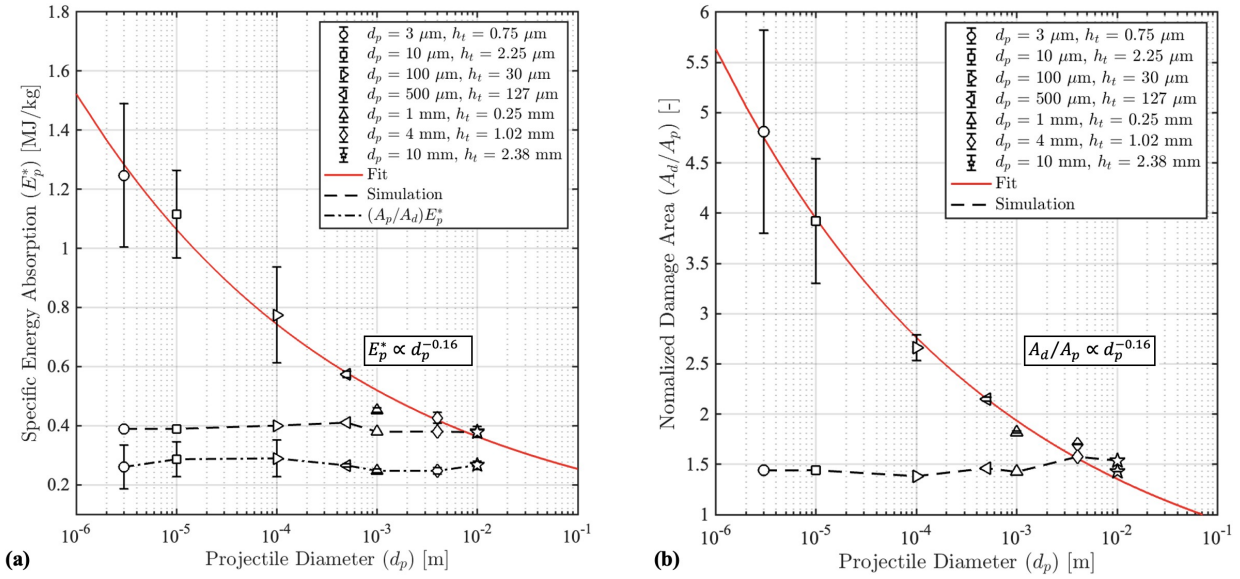

Figure 9: Key impact experiment results as a function of length scale (projectile diameter): (a) specific energy absorption, Eq. (2), and (b) normalized deformation area, Eq. (4). Both metrics follow similar power law trends, decreasing dramatically with length scale. Also included are damage-area-normalized E_p^* values $[(A_p/A_d)E_p^*]$, as well as EPIC code predictions for E_p^* and A_d/A_p.

An alternative approach to normalizing impact energy absorption (E_p) is by employing the deformation area rather than the projectile's projected area [*i.e.*, $(A_p/A_d)E_p^*$]. Interestingly, these deformation-area-normalized E_p values remain largely constant across the different scales (see Fig. 9a; dash-dot line). These findings reveal that (i) relative target features resulting from impact-induced deformation and failure lack some consistency across length scale, even when the projectile/target materials and geometries and the impact velocity are unchanged, and (ii) the added volume of target material undergoing deformation as length scale decreases $[(A_d - A_p)h_t]$ is responsible (through plastic work, heating, *etc.*) for the rise in E_p^*.

The complementary numerical impact simulations ($v_i \equiv 550$ m/s and $h_t/d_p \equiv 0.25$) were used to approximate the projectile residual velocity (v_r) at each length scale. The simulation methodology, material models, and model parameters are provided in Supplementary Information, Sect. SI.6. The simulated v_i and v_r values were then used with Eq. (2) to arrive at predicted specific energy absorption (E_p^*) values (see Fig. 9a, dashed line). The simulations fail to reflect the experimental rise in E_p^* with decreasing projectile diameter (d_p). The EPIC simulations were also used to predict changes in normalized deformation area with scale, as shown in Fig. 9b. These predictions are based on the diameter D of a circular region encompassing all out-of-plane target deformation quantified using the same method described in Fig. 6d and Eq. (4). Similar to the E_p^* calculations, EPIC predicts negligible change in A_d/A_p. The failure of advanced impact simulation techniques to predict *any* noticeable increase in E_p^* or A_d/A_p underscores a knowledge gap in understanding how impact behavior varies from the macroscale (10^{-2} m) to the microscale (10^{-6} m).

With smaller length scales, there is a dramatic increase in local strain and heating rates driven by a reduction in the duration of the penetration/perforation event. This rate escalation may substantially enhance or degrade local material properties and/or trigger different primary failure and energy dissipation mechanisms, leading to relatively higher projectile energy absorption. Specifically, event durations decrease from ∼100 µs to ∼100 ns (by 1,000 times) when moving from larger to smaller length scales. This temporal reduction potentially inhibits some failure mechanisms from contributing to smaller-scale energy absorption, while activating or enhancing the contribution of others. One simple approach to estimating the nominal strain rate within the target involves using an analytical expression, such as that derived by Lee *et al.* [31]:

$$\dot{\bar{\varepsilon}} = \frac{t_p}{2}\left(\frac{v_i}{R_c}\right)^2, \tag{5}$$

where t_p is the perforation/puncture time, $R_c \approx v_c t_p$ is the cone radius, $v_c \approx 1.23 c_{||}(v_i/\sqrt{2}c_{||})^{2/3}$ is the cone velocity [78], $c_{||} = \sqrt{E^*/\rho_t}$ is the in-plane wave speed, and $E^* = E/(1-\nu^2)$ is the plain-strain elastic modulus. For simplicity, the puncture time was approximated as $t_p \approx h_t/v_i$. Equation (5) is plotted as a function of film thickness in Fig. 10, which illustrates a four order of magnitude increase in nominal strain rate from the largest to smallest scale. The increase in local strain rates were also captured in the scaled impact simulations. The *maximum* simulated equivalent plastic strain rates ($\max \dot{\varepsilon}_{eq}$) are also included in the plot for comparison. They were on average roughly 140 times greater than the *nominal* analytical $\dot{\bar{\varepsilon}}$ values. In general, instantaneous material properties can be substantially affected by the strain and heating rates. For PC, as with many materials, an increase in strain rate can enhance several properties, including yield stress and elastic modulus [79, 80]. This enhancement, however, can be offset by adiabatic-heating-induced thermal softening resulting from shock propagation and/or plastic work. Impact-induced temperatures can exceed the glass transition or melt temperature of the material, activating potentially higher energy absorbing deformation and failure mechanisms. This interplay likely contributed to the observed increase in specific energy absorption and normalized deformation area, as depicted in Fig. 9.

A further point to consider is the potential introduction of *molecular* anisotropy in the LIPIT samples resulting from their notably thin structure (h_t = 0.75, 2.25 µm). Such anisotropy could alter dynamic material behavior and failure in a way that favors energy absorption, contributing to the observed increases in E_p^* and A_d/A_p with decreasing scale (Fig. 9). The influence of molecular anisotropy, however, is unlikely due to the substantial size difference between the average PC molecule and even the thinnest target. For instance, the volume of the h_t = 0.75 µm target material beneath the projectile before impact ($\pi/4\, d_p^2 h_t$) is over one hundred thousand times greater than the volume of a sphere enclosing the average PC chain as defined by its root-mean-square end-to-end distance (see Supplementary Information, Sect. SI.1) [81].

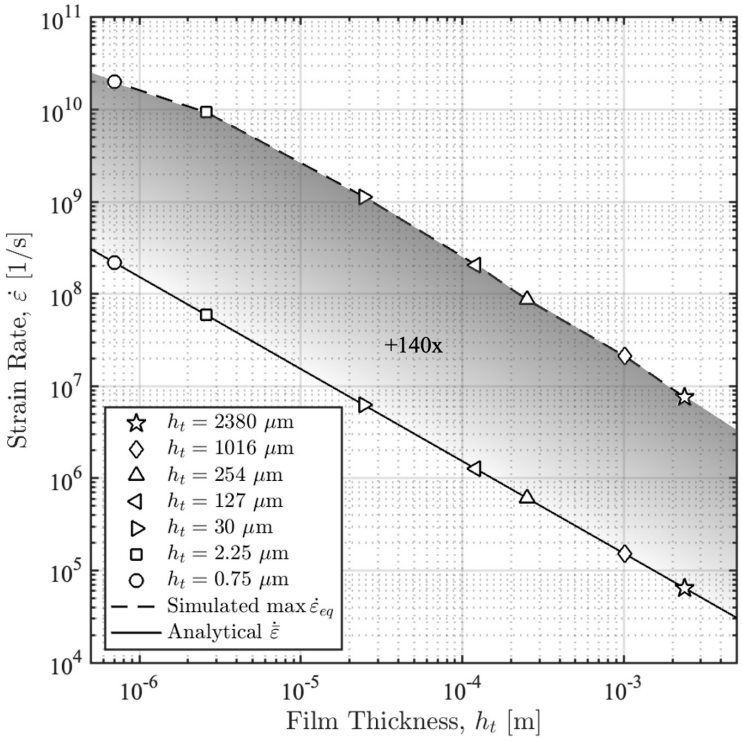

Figure 10: Nominal target film strain rate [*cf.* Eq. (5)] as a function of its thickness, h_t [31, 78]. Strain rate increases by roughly four orders of magnitude from the largest to smallest length scale.

Furthermore, while surface effects can depress T_g as films become thinner, these effects have a negligible influence on the bulk material T_g for linear glassy polymers until film thicknesses reach $h_t \approx 100$ nm (∼87% thinner than the thinnest $h_t = 750$ nm film) [82, 83]. These considerations show that any thickness-induced molecular anisotropy effects (if present) are overwhelmed by the projectile and do not effect energy absorption. Residual internal stresses in the PC targets caused by material manufacturing and processing might also affect impact energy absorption and deformation, particularly at smaller scales. The spin-coating and compression-molding sample preparation techniques, however, did not introduce any noticeable material anisotropy, as evidenced by cross-polarizing microscopy (refer to Supplementary Information, Sect. SI.5).

Despite the material models used [Eqs. (S5), (S6), and (S7)] being sensitive to strain rates and temperature, they do not accurately replicate the experimental target response. This disagreement exists although simulated strain rates are nominally consistent with expected experimental values (*i.e.*, they grow by orders of magnitude). Most high-rate material models are calibrated using experimental results from Split-Hopkinson Bar tests at strain rates up to 10^4 s^{-1}—but this is over four orders of magnitude less than nominal LIPIT values [84]. Moreover, sample test temperatures typically do not exceed roughly 200°C for polymers. Therefore, a likely explanation for the discrepancy between the simulated and experimental E_p^* values could be that the material models and EOS employed are not designed and/or calibrated for the specific impact con-

ditions under investigation. Even so, calibrating existing established material models will be an insufficient approach: closing the gap in understanding may require the development of entirely new material models or computational approaches that accurately capture scale-induced changes in predominant material deformation behavior, phase transformations, and failure mechanisms that are negligible/overwhelmed at larger scales. These issues are discussed in more detail in the Supplementary Information, Sect. SI.7.

Post-experiment, the impacted PC samples were immediately sealed at room temperature to preserve the deformation and minimize contamination. Subsequent examinations of the impact and exit surfaces were conducted with optical and laser confocal microscopy (*cf.* Fig. 7). Figure 11 offers a visual comparison of the damage from alumina sphere impacts of diameters $d_p = 0.5$, 1, 4, 10 mm, arranged in descending order. Figures 11a, 11c, 11e, and 11g illustrate the impact sides of the perforated films, and Figs. 11b, 11d, 11f, and 11h depict the exit sides. Each image includes a superimposed yellow dashed circle representing the projectile's projection and a scale bar positioned in the bottom right corner. Similarly, optical micrographs of the remaining perforations ($d_p = 3$, 10, 100 μm) are displayed in Fig. 12 using the same layout. In all experiments, the damaged area exceeded the projectile's projected area ($A_d/A_p > 1$; *cf.* Fig. 9b). The effective diameter of the perforation hole/opening was consistently smaller than that of the projectile, suggesting a degree of hole closure post-perforation, akin to material "self-healing" [85, 86]. Notably, the perforations from projectiles of 4 mm (Figs. 11a and 11b) and 100 μm (Figs. 12a and 12b) diameters seemed completely closed, possibly due to slightly larger h_t/d_p ratios. Minimal out-of-plane deformation was observed on the impact face, in contrast to the significant deformation on the exit face across all considered length scales. Signs of jetting, the ejection of material from the impactor-target contact point, were present (Figs. 11e–11h), while there was little to no evidence of large-scale shear banding, crazing, or cracking. The apparent absence of these features might be due to adiabatic heating elevating temperatures above T_g, leading to substantial visco-plastic flow that concealed them. In fact, evidence of material flow was present in all micrographs. A slightly higher degree of surface roughness was present in the $h_t = 25$ μm target sample ($d_p = 100$ μm) due to the compression molding process (Figs. 12a and 12b); however, with nominal peak-to-valley distances being less than $0.01d_p$, the experimental results were likely unaffected. Although the geometry and regularity of the perforations appear to vary with scale, the micrographs do not show any obvious changes in primary failure mechanisms or material behavior, such as ductile to brittle transitions. Figures 11 and 12, however, do visually demonstrate the growth of the deformation area (A_d) relative to the projectile's projected area (A_p) as the length scale decreases.

The apparent concentric rings visible in the $d_p = 10$ μm (Figs. 12c and 12d) and $d_p = 3$ μm (Figs. 12e and 12f) perforation images are optical artifacts, likely arising from the perforation dimensions being near the limit of the Keyence microscope's resolution capabilities. For this reason, optical microscopy of

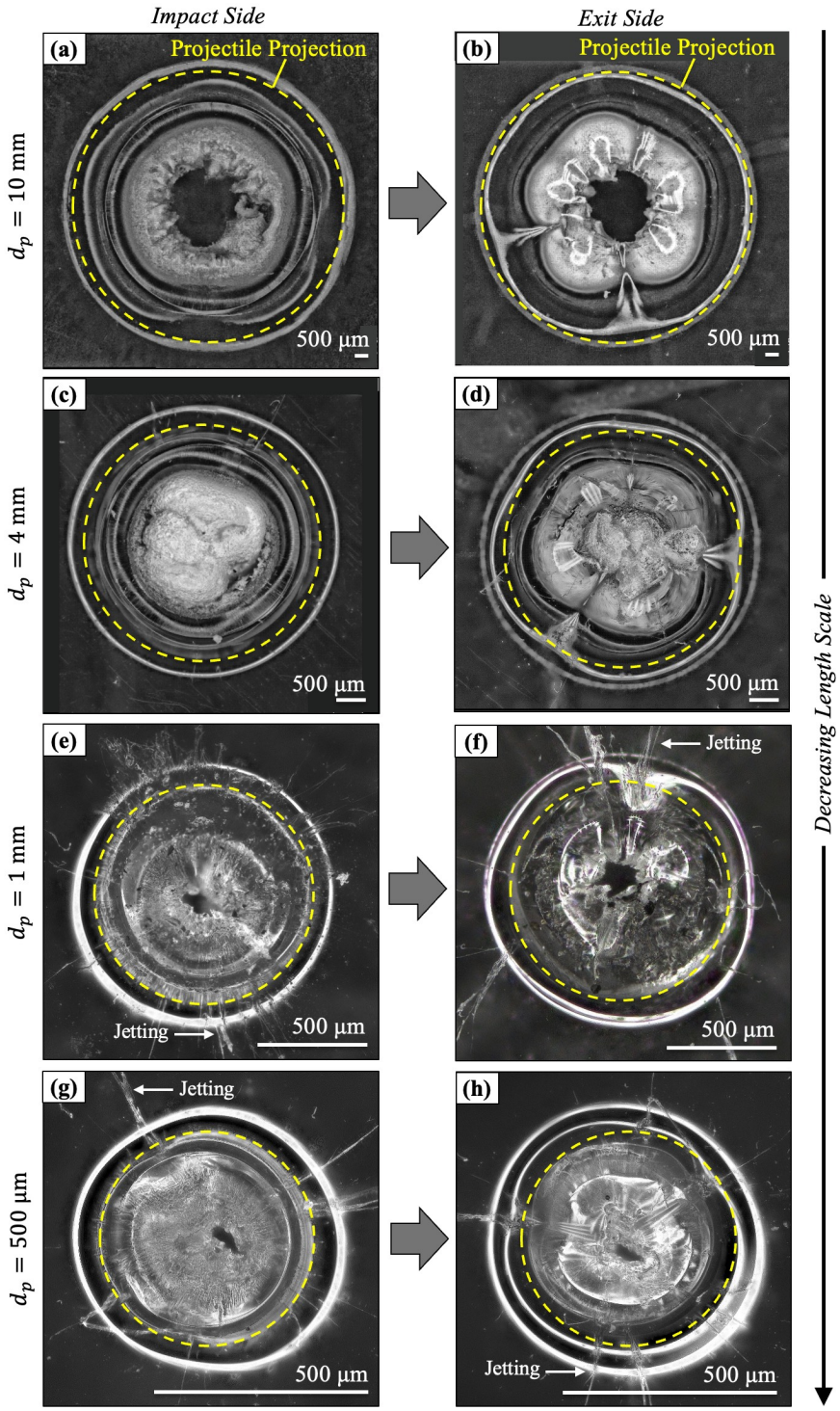

Figure 11: Orthogonal micrographs (along impact axis) display perforations in the PC targets caused by impacts from alumina spheres with diameters of (a, b) $d_p = 10$ mm, (c, d) $d_p = 4$ mm, (e, f) $d_p = 1$ mm, and (g, h) $d_p = 0.5$ mm. Within the array of images, the left column (a, c, e, g) represents the impact face of the target, whereas the right column (b, d, f, h) depicts the exit face. On each micrograph, a 2D projection of the projectile is overlaid, indicated by a dashed yellow line, to serve as a point of reference.

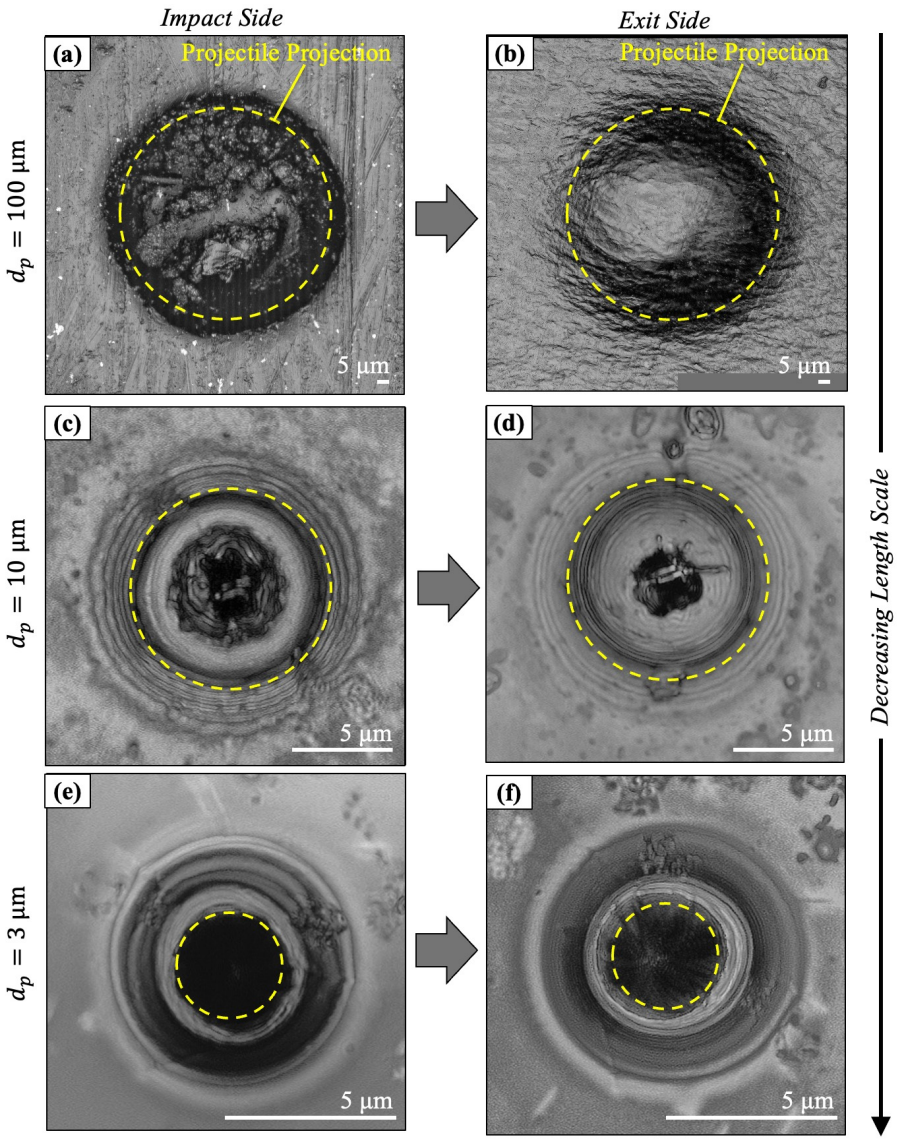

Figure 12: Orthogonal micrographs (along impact axis) display perforations in the PC targets caused by impacts from alumina spheres with diameters of (a, b) $d_p = 100$ µm, (c, d) $d_p = 10$ µm, and (e, f) $d_p = 3$ µm. Within the array of images, the left column (a, c, e) represents the impact face of the target, whereas the right column (b, d, f) depicts the exit face. On each micrograph, a 2D projection of the projectile is overlaid, indicated by a dashed yellow line, to serve as a point of reference.

the LIPIT samples was supplemented with SEM to obtain images that better show the physical features of the $d_p = 10$ µm and $d_p = 3$ µm perforations. Orthogonal images of the front (impact) and back sides of the thin films were captured for the same $d_p = 10$ µm (Figs. 13a and 13b) and $d_p = 3$ µm (Figs. 13e and 13f) perforations originally shown in Figs. 12c and 12d and Figs. 12e and 12f, respectively. Again, the yellow dashed circle superimposed on each image highlights the corresponding projectile's size relative to the perforation. The concentric rings visible in the optical micrographs clearly do not appear in the SEM images. Isometric SEM images at a 48° angle from the film plane were taken of both the same $d_p = 10$ µm (Figs. 13c and 13d) and $d_p = 3$ µm (Figs. 13g and 13h) projectile perforations to better highlight the

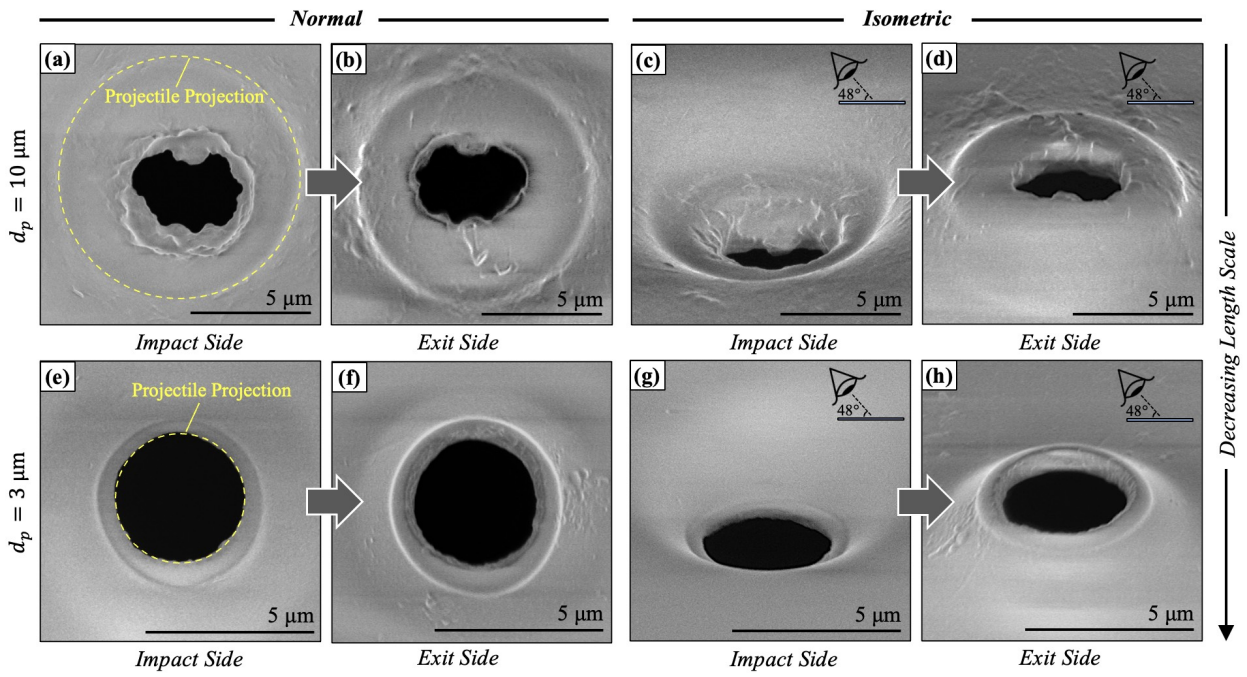

Figure 13: Orthogonal (90°) and isometric (48°) SEM images of the PC target perforations resulting from LIPIT impacts from alumina spheres with diameters of (a–d) $d_p = 10$ µm and (e–h) $d_p = 3$ µm. For each viewing perspective, an (a, c, e, g) impact side and exit side (b, d, f, h) image is shown. On each normal micrograph, a 2D projection of the projectile is overlaid, indicated by a dashed yellow line, to serve as a point of reference.

perforation geometry and deformation features not evident in the normal SEM images. The relatively large conical perforation geometries seen in the isometric scans were characteristic of the LIPIT samples (more later) and are in general agreement with previous LIPIT results for PC thin films [49]. Perforation hole geometries and effective deformation areas in the SEM images aligned with those of the optical micrographs.

Another objective of this study was to probe scale-induced changes in perforation geometry. The OM and SEM images in Figs. 11–13 offer only limited quantitative data on the cross-sectional perforation geometries, so laser confocal microscopy was employed to collect profilometry data on both the front and back surfaces of the perforations at each length scale. To facilitate comparison and visualization, the front and back side 1D profiles were normalized using the projectile diameter (d_p) and shifted by the appropriate average h_t/d_p ratio (*cf.* Table 1). This normalized representative two-dimensional (2D) cross-sectional profiles, as shown in descending order in Fig. 14. These cross sections are annotated with corresponding d_p and h_t values and highlighted with distinct colors. Matching microscopy images (*cf.* Figs. 11–13) are provided for reference on the right, with the imaging method noted at the top left of each micrograph. A scaled projectile profile ($d_p/d_p = 1$) moving downward at velocity v_r is depicted at the bottom of the plot, illustrating that the normalized effective deformation area increases as the length scale decreases ($A_d/A_p \propto 1/d_p$). The figure also clearly shows that the perforation openings are consistently smaller than the projectile. Interestingly, the thicker specimens exhibit signs of plugging failure behavior, while the thinner specimens seem to undergo

more bulk bending deformation (dishing) [46]. More extensive dishing could lead to a proportionally higher degree of energy absorption because it involves substantial plastic deformation over a larger area, while plugging tends to be more localized and less deformative. This transition in the predominant failure mode with decreasing length scale could partially explain the observed enhancement in E_p^* (*cf.* Fig. 9a).

4. Conclusions

When the length scale decreases from centimeters to microns, the dynamic behavior of materials can dramatically change due to corresponding modifications in event duration, strain and heating rates, material inhomogeneities, among other factors. Addressing this issue is vital to the success of emerging high-throughput material characterization techniques. The Laser-Induced Particle Impact Test (LIPIT) has proven to be a valuable method for studying high strain rate deformation of various materials at the microscale, thanks to its precision, minimal lab space requirement, and high-throughput testing capacity. Initial observations from LIPIT indicate that microscale energy absorption can exceed macroscale results by over a decade. This current study intentionally probes geometric scaling effects on dynamic material behavior by using a LIPIT apparatus and a single-stage light gas gun to launch noncrystalline alumina spheres of 3, 10, 100, 500, 1,000, 4,000, and 10,000 μm in diameter into scaled $h_t/d_p = 0.25$ polycarbonate (PC) targets. The results of these experiments, ranging in impact energies from hundreds of joules down to just nanojoules, suggest that decreasing length scale alone *for the same projectile and target materials and geometries* results in a dramatic 230% increase in energy absorption and a corresponding 240% rise in normalized deformation area. Microscopic and profilometric analysis of the PC perforations offers insights into potential transitions in deformation and failure behavior with decreasing scale. Complementary advanced numerical simulations of these impacts, however, do not show any increase in specific energy absorption or normalized deformation area even though predicted strain rates reflect expected values. Such discrepancies underscore the limitations of current material models when scaling down impacts from macroscale (10^{-2} m) to microscale (10^{-6} m). Experimental and simulation design, implementation, and analysis would be complicated by the introduction of material hierarchical inhomogeneities, such as those present in metals, carbon nanotube mats, *etc.* The findings of this study strongly suggest that length scale cannot be ignored in both developing and applying established and innovative microscale material characterization techniques, particularly for advanced material discovery. For these reasons, one key goal of this study is to stimulate scientific dialogue and begin developing a framework for investigating how geometric scale affects impact phenomena.

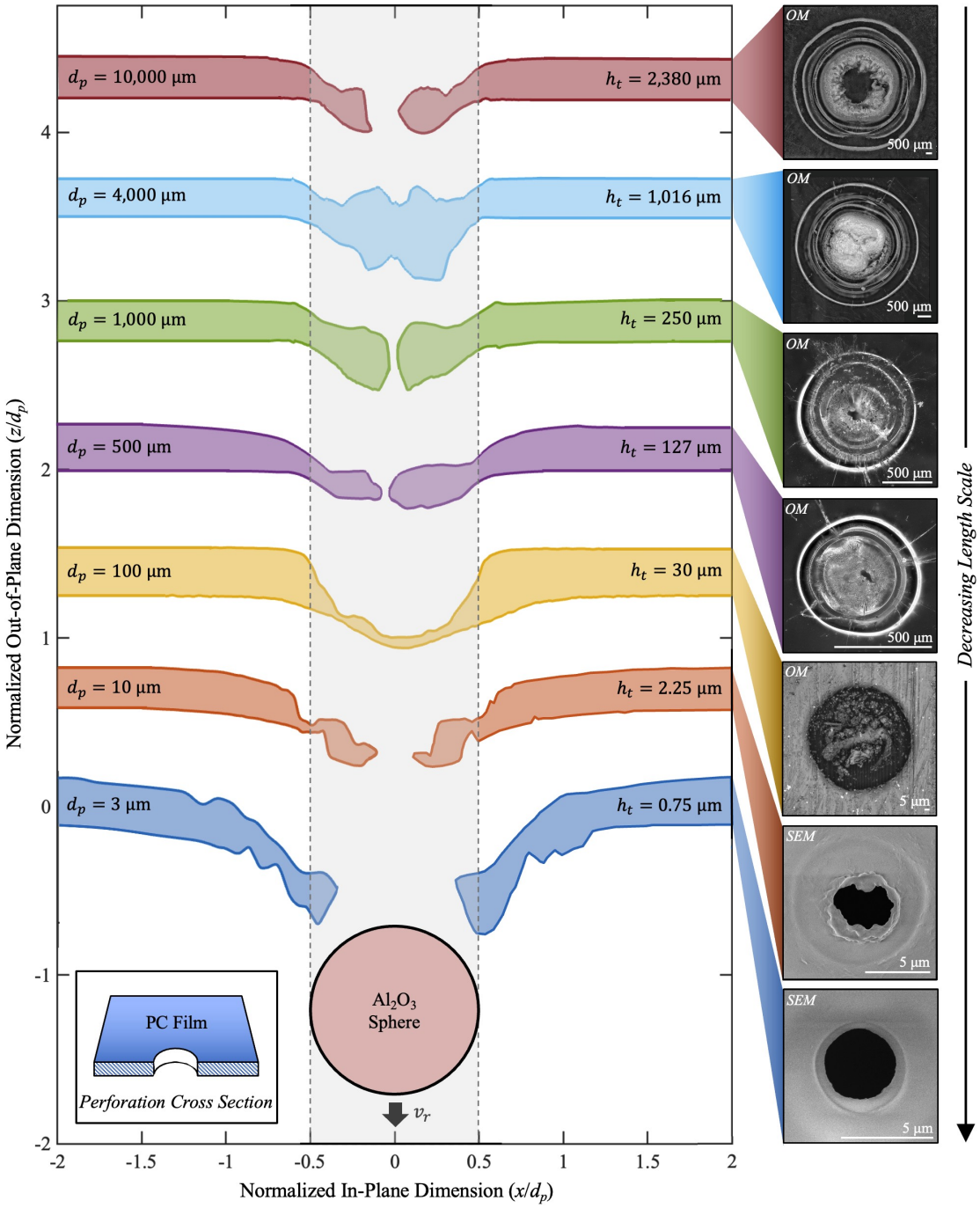

Figure 14: Representative *experimental* one-dimensional cross-sectional profiles of the perforated PC target samples (hatched region, figure inset). All profile data was captured using laser confocal microscopy and normalized by the respective projectile diameter (d_p) for comparison across length scales. At each scale, impact and exit side profiles (dark solid lines) are displaced by the corresponding h_t/d_p values provided in Table 1 for ease of visualization. An *impact side* micrograph of the target perforation is shown for each cross-sectional profile, with the microscopy technique noted in the top left corner: optical microscopy (OM) or scanning electron microscopy (SEM). Length scale decreases from top to bottom. Vertical dashed lines show the projectile diameter ($d_p/d_p = 1$) relative to the perforation regions: normalized effective deformation area [A_d/A_p; Eq. (4)] grows with decreasing length scale.

Acknowledgments

This research is based upon work partially supported by the National Science Foundation (NSF) Graduate Research Fellowship under Grant No. 1746932. A portion of this research was also sponsored by the Army Research Laboratory and was accomplished under Cooperative Agreement Number W911NF-22-2-0106. The views and conclusions contained in this document are those of the authors and should not be interpreted as representing the official policies, either expressed or implied, of the Army Research Laboratory or the U.S. Government. The U.S. Government is authorized to reproduce and distribute reprints for Government Purposes notwithstanding any copyright notation herein.

Use of the Texas A&M University Soft Matter Facility (RRID:SCR_022482) and contribution of Dr. Peiran Wei are acknowledged. Use of the Texas A&M University Microscopy and Imaging Center Core Facility (RRID:SCR_022128) and contribution of Dr. Stanislav Vitha are also acknowledged. Gavin Lukasik assisted with the set up and alignment of the Infinity K2 Distamax long distance microscope with a CF2 objective used for the $d_p = 100$ μm and $d_p = 500$ μm SSGG experiments. Zhen Sang performed a subset of the SEM imaging of the PC target perforations following the LIPIT experiments.

References

[1] D. L. Block *et al.*, "An almost head-on collision as the origin of two off-centre rings in the andromeda galaxy," *Nature*, vol. 443, no. 7113, pp. 832–834, 2006.

[2] T. Cox and A. Loeb, "The collision between the milky way and andromeda," *Monthly Notices of the Royal Astronomical Society*, vol. 386, no. 1, pp. 461–474, 2008.

[3] P. Schulte *et al.*, "The chicxulub asteroid impact and mass extinction at the cretaceous-paleogene boundary," *Science*, vol. 327, no. 5970, pp. 1214–1218, 2010.

[4] S. N. Patek *et al.*, "Deadly strike mechanism of a mantis shrimp," *Nature*, vol. 428, no. 6985, pp. 819–820, 2004.

[5] M. Arnould *et al.*, "The r-process of stellar nucleosynthesis: Astrophysics and nuclear physics achievements and mysteries," *Physics Reports*, vol. 450, no. 4-6, pp. 97–213, 2007.

[6] J.-Y. Li *et al.*, "Ejecta from the dart-produced active asteroid dimorphos," *Nature*, pp. 1–3, 2023.

[7] M. Kobayashi *et al.*, "Mechanism of creation of compressive residual stress by shot peening," *International Journal of Fatigue*, vol. 20, no. 5, pp. 351–357, 1998.

[8] R. Stone, "Need for speed," *Science*, vol. 367, no. 6474, pp. 134–138, 2020. DOI: 10.1126/science.367.6474.134. eprint: https://www.science.org/doi/pdf/10.1126/science.367.6474.134. [Online]. Available: https://www.science.org/doi/abs/10.1126/science.367.6474.134.

[9] L. Metz *et al.*, "Bow-and-arrow, technology of the first modern humans in europe 54,000 years ago at mandrin, france," *Science Advances*, vol. 9, no. 8, eadd4675, 2023. DOI: 10.1126/sciadv.add4675. eprint: https://www.science.org/doi/pdf/10.1126/sciadv.add4675. [Online]. Available: https://www.science.org/doi/abs/10.1126/sciadv.add4675.

[10] A. A. Tiamiyu and C. A. Schuh, "Particle flattening during cold spray: Mechanistic regimes revealed by single particle impact tests," *Surface and Coatings Technology*, vol. 403, p. 126 386, 2020.

[11] D. Veysset *et al.*, "High-velocity micro-particle impact on gelatin and synthetic hydrogel," *Journal of the mechanical behavior of biomedical materials*, vol. 86, pp. 71–76, 2018.

[12] A. Zylstra *et al.*, "Experimental achievement and signatures of ignition at the national ignition facility," *Physical Review E*, vol. 106, no. 2, p. 025 202, 2022.

[13] M. A. Abtew *et al.*, "Ballistic impact mechanisms–a review on textiles and fibre-reinforced composites impact responses," *Composite structures*, vol. 223, p. 110 966, 2019.

[14] M. D. Pearlman, D. Viano, *et al.*, "Automobile crash simulation with the first pregnant crash test dummy," *American journal of obstetrics and gynecology*, vol. 175, no. 4, pp. 977–981, 1996.

[15] E. L. Christiansen and J. H. Kerr, "Mesh double-bumper shield: A low-weight alternative for spacecraft meteoroid and orbital debris protection," *International Journal of Impact Engineering*, vol. 14, no. 1-4, pp. 169–180, 1993.

[16] K. A. Holsapple, "The scaling of impact phenomena," *International Journal of Impact Engineering*, vol. 5, no. 1-4, pp. 343–355, 1987.

[17] Department of Defense, *MIL-STD-662F, Department of Defense Test Method Standard, V50 Ballistic Test for Armor*, Department of Defense Standard, 1997.

[18] M. E. Backman and W. Goldsmith, "The mechanics of penetration of projectiles into targets," *International Journal of Engineering Science*, vol. 16, no. 1, pp. 1–99, 1978.

[19] J. D. Walker, *Modern impact and penetration mechanics*. Cambridge university press, 2021.

[20] M. A. Meyers *et al.*, "The effect of grain size on the high-strain, high-strain-rate behavior of copper," *Metallurgical and materials transactions A*, vol. 26, pp. 2881–2893, 1995.

[21] K. A. Holsapple, "The scaling of impact processes in planetary sciences," *Annual review of earth and planetary sciences*, vol. 21, no. 1, pp. 333–373, 1993.

[22] D. Littlefield *et al.*, "Geometric and energy scaling for celestial impacts," *International Journal of Impact Engineering*, vol. 35, no. 12, pp. 1642–1647, 2008.

[23] G. L. Ferguson, "Replica model scaling for high strain-rate events," *International journal of impact engineering*, vol. 16, no. 4, pp. 571–583, 1995.

[24] Y Peng *et al.*, "Geometrical scaling effect for penetration depth of hard projectiles into concrete targets," *International Journal of Impact Engineering*, vol. 120, pp. 46–59, 2018.

[25] P. S. Westine and S. A. Mullin, "Scale modeling of hypervelocity impact," *International Journal of Impact Engineering*, vol. 5, no. 1-4, pp. 693–701, 1987.

[26] G. M. Pharr *et al.*, "The indentation size effect: A critical examination of experimental observations and mechanistic interpretations," *Annual Review of Materials Research*, vol. 40, pp. 271–292, 2010.

[27] A. Reiser and C. A. Schuh, "Microparticle impact testing at high precision, higher temperatures, and with lithographically patterned projectiles," *Small Methods*, vol. 7, no. 1, p. 2 201 028, 2023.

[28] K. E. Brown *et al.*, "Simplified laser-driven flyer plates for shock compression science," *Review of Scientific Instruments*, vol. 83, no. 10, p. 103 901, 2012.

[29] J.-H. Lee *et al.*, "High strain rate deformation of layered nanocomposites," *Nature communications*, vol. 3, no. 1, p. 1164, 2012.

[30] D. Veysset *et al.*, "Dynamics of supersonic microparticle impact on elastomers revealed by real–time multi–frame imaging," *Scientific reports*, vol. 6, no. 1, p. 25 577, 2016.

[31] J.-H. Lee *et al.*, "Dynamic mechanical behavior of multilayer graphene via supersonic projectile penetration," *Science*, vol. 346, no. 6213, pp. 1092–1096, 2014.

[32] W. Xie *et al.*, "Dynamics and extreme plasticity of metallic microparticles in supersonic collisions," *Scientific reports*, vol. 7, no. 1, p. 5073, 2017.

[33] J. Cai and R. Thevamaran, "Superior energy dissipation by ultrathin semicrystalline polymer films under supersonic microprojectile impacts," *Nano letters*, vol. 20, no. 8, pp. 5632–5638, 2020.

[34] S. H. Chen *et al.*, "Using microprojectiles to study the ballistic limit of polymer thin films," *Soft Matter*, vol. 16, no. 16, pp. 3886–3890, 2020.

[35] D. Veysset *et al.*, "High-velocity micro-projectile impact testing," *Applied Physics Reviews*, vol. 8, no. 1, p. 011 319, 2021.

[36] S. Imbriglio *et al.*, "Adhesion strength of titanium particles to alumina substrates: A combined cold spray and lipit study," *Surface and Coatings Technology*, vol. 361, pp. 403–412, 2019.

[37] Y. Peng *et al.*, "Extreme strain rate deformation of nacre-inspired graphene/copper nanocomposites under laser-induced hypersonic micro-projectile impact," *Composites Part B: Engineering*, vol. 235, p. 109 763, 2022.

[38] J. Dong *et al.*, "Impact resistance of single-layer metallic glass nanofilms to high-velocity micro-particle penetration," *Extreme Mechanics Letters*, vol. 44, p. 101 258, 2021.

[39] J. Hyon *et al.*, "Extreme energy dissipation via material evolution in carbon nanotube mats," *Advanced Science*, vol. 8, no. 6, p. 2 003 142, 2021.

[40] W. Shan *et al.*, "Layered thin film deposition via extreme inter-brush slip in a lamellar block copolymer," *Macromolecules*, vol. 55, no. 20, pp. 9022–9029, 2022.

[41] W. Shan *et al.*, "Influence of entanglements on ultrahigh strain rate deformation of polystyrene microprojectiles," *Macromolecules*, vol. 55, no. 21, pp. 9594–9600, 2022.

[42] J. Hyon *et al.*, "Extreme energy absorption in glassy polymer thin films by supersonic micro-projectile impact," *Materials Today*, vol. 21, no. 8, pp. 817–824, 2018.

[43] K. Callahan *et al.*, "High strain rate failure behavior of polycarbonate plates due to hypervelocity impact," *Macromolecules*, vol. 55, no. 21, pp. 9640–9649, 2022.

[44] Y. Bian *et al.*, "High-speed penetration dynamics of polycarbonate," *International Journal of Mechanical Sciences*, vol. 223, p. 107 250, 2022.

[45] N. Kawai *et al.*, "In-situ observation of damage evolution in polycarbonate subjected to hypervelocity impact," *International Journal of Impact Engineering*, vol. 142, p. 103 584, 2020.

[46] S. Wright *et al.*, "Ballistic impact of polycarbonate-an experimental investigation," *International Journal of Impact Engineering*, vol. 13, no. 1, pp. 1–20, 1993.

[47] A Dorogoy *et al.*, "Experimentation and modeling of inclined ballistic impact in thick polycarbonate plates," *International Journal of Impact Engineering*, vol. 38, no. 10, pp. 804–814, 2011.

[48] R. R. Burt and E. L. Christiansen, "Hypervelocity impact testing of transparent spacecraft materials," *International Journal of Impact Engineering*, vol. 29, no. 1-10, pp. 153–166, 2003.

[49] E. P. Chan *et al.*, "Entanglement density-dependent energy absorption of polycarbonate films via supersonic fracture," *ACS Macro Letters*, vol. 8, no. 7, pp. 806–811, 2019.

[50] C. R. Siviour and J. L. Jordan, "High strain rate mechanics of polymers: A review," *Journal of Dynamic Behavior of Materials*, vol. 2, pp. 15–32, 2016.

[51] C Bauwens-Crowet *et al.*, "Tensile yield-stress behavior of glassy polymers," *Journal of Polymer Science Part A-2: Polymer Physics*, vol. 7, no. 4, pp. 735–742, 1969.

[52] C Bauwens-Crowet *et al.*, "The temperature dependence of yield of polycarbonate in uniaxial compression and tensile tests," *Journal of Materials Science*, vol. 7, pp. 176–183, 1972.

[53] Z. Li and J. Lambros, "Strain rate effects on the thermomechanical behavior of polymers," *International Journal of solids and structures*, vol. 38, no. 20, pp. 3549–3562, 2001.

[54] D. Legrand, "Crazing, yielding, and fracture of polymers. i. ductile brittle transition in polycarbonate," *Journal of applied polymer science*, vol. 13, no. 10, pp. 2129–2147, 1969.

[55] S. Sarva *et al.*, "Mechanics of taylor impact testing of polycarbonate," *International Journal of Solids and Structures*, vol. 44, no. 7-8, pp. 2381–2400, 2007.

[56] N. A. Fleck *et al.*, "High strain-rate shear response of polycarbonate and polymethyl methacrylate," *Proceedings of the Royal Society of London. A. Mathematical and Physical Sciences*, vol. 429, no. 1877, pp. 459–479, 1990.

[57] E. L. Thomas and S. J. Israel, "Microstructure of crazes in solvent-crazed polycarbonate thin films," *Journal of Materials Science*, vol. 10, pp. 1603–1607, 1975.

[58] R. J. Morgan and J. E. O'Neal, "Modes of deformation and failure of polycarbonate," *Polymer*, vol. 20, no. 3, pp. 375–387, 1979.

[59] S. M. Aharoni, "Correlations between chain parameters and failure characteristics of polymers below their glass transition temperature," *Macromolecules*, vol. 18, no. 12, pp. 2624–2630, 1985.

[60] A. M. Donald and E. J. Kramer, "Effect of molecular entanglements on craze microstructure in glassy polymers," *Journal of Polymer Science: Polymer Physics Edition*, vol. 20, no. 5, pp. 899–909, 1982.

[61] A. M. Donald and E. J. Kramer, "The competition between shear deformation and crazing in glassy polymers," *Journal of Materials Science*, vol. 17, pp. 1871–1879, 1982.

[62] R. N. Haward, *The physics of glassy polymers*. Springer Science & Business Media, 2012.

[63] P. G. Whitten and H. R. Brown, "Polymer entanglement density and its influence on interfacial friction," *Physical Review E*, vol. 76, no. 2, p. 026 101, 2007.

[64] M. Kendall and C. Siviour, "Experimentally simulating high-rate behaviour: Rate and temperature effects in polycarbonate and pmma," *Philosophical Transactions of the Royal Society A: Mathematical, Physical and Engineering Sciences*, vol. 372, no. 2015, p. 20 130 202, 2014.

[65] Z. Gu *et al.*, "Geometrical scaling law for laser-induced micro-projectile impact testing," *International Journal of Mechanical Sciences*, vol. 223, p. 107 289, 2022.

[66] Z. Meng and S. Keten, "Unraveling the effect of material properties and geometrical factors on ballistic penetration energy of nanoscale thin films," *Journal of Applied Mechanics*, vol. 85, no. 12, p. 121 004, 2018.

[67] R. Thevamaran *et al.*, "Dynamic creation and evolution of gradient nanostructure in single-crystal metallic microcubes," *Science*, vol. 354, no. 6310, pp. 312–316, 2016.

[68] J. A. Rogers *et al.*, "The texas a&m university hypervelocity impact laboratory: A modern aeroballistic range facility," *Review of Scientific Instruments*, vol. 93, no. 8, p. 085 106, 2022.

[69] J. A. Rogers *et al.*, "Mechanics of hypervelocity simultaneously launched distributed particles," *International Journal of Impact Engineering*, 2023.

[70] *Tuffak® gp polycarbonate sheet*, 2022, p. 2. [Online]. Available: `https://plaskolite.com/docs/default-source/tuffak-assets/product-data-sheets/pds004_gp.pdf`.

[71] *Rowtec® pc1 graphic arts polycarbonate film*, 2023, p. 2. [Online]. Available: `https://www.orafol.com/fileadmin/americas/images/literature/rowland_apf_-_tables/rowtec/rowtec-pc1_table.pdf`.

[72] *Shimadzu hyper vision hpv-x2*, 2017, p. 2. [Online]. Available: https://hadlandimaging.com/wp-content/uploads/2021/12/HADLAND-Shimadzu-HPV-X2-brochure-v2a.pdf.

[73] *Rel sure-bright profusion x gen2 led lighting system*, 2019, p. 2. [Online]. Available: https://hadlandimaging.com/rel-ws-led-series/#WS3.

[74] *Specialized imaging simx*, p. 2. [Online]. Available: https://www.specialised-imaging.com/application/files/6416/4816/0060/SI_SIMX_01_Q02_A4.pdf.

[75] D. Brown *et al.*, *Tracker video analysis and modeling tool for physics education (v6.1.5)*, 2023. [Online]. Available: https://physlets.org/tracker/.

[76] C. A. Schneider *et al.*, "Nih image to imagej: 25 years of image analysis," *Nature methods*, vol. 9, no. 7, pp. 671–675, 2012.

[77] J. Hyon *et al.*, "Projectile impact shock-induced deformation of one-component polymer nanocomposite thin films," *ACS nano*, vol. 15, no. 2, pp. 2439–2446, 2021.

[78] S. L. Phoenix and P. K. Porwal, "A new membrane model for the ballistic impact response and v50 performance of multi-ply fibrous systems," *International Journal of Solids and Structures*, vol. 40, no. 24, pp. 6723–6765, 2003.

[79] U. A. Dar *et al.*, "Thermal and strain rate sensitive compressive behavior of polycarbonate polymer-experimental and constitutive analysis," *Journal of Polymer Research*, vol. 21, pp. 1–10, 2014.

[80] K. Cao *et al.*, "Effects of strain rate and temperature on the tension behavior of polycarbonate," *Materials & Design*, vol. 38, pp. 53–58, 2012.

[81] L. Fetters *et al.*, "Connection between polymer molecular weight, density, chain dimensions, and melt viscoelastic properties," *Macromolecules*, vol. 27, no. 17, pp. 4639–4647, 1994.

[82] P. A. O'Connell *et al.*, "Exceptional property changes in ultrathin films of polycarbonate: Glass temperature, rubbery stiffening, and flow," *Macromolecules*, vol. 45, no. 5, pp. 2453–2459, 2012.

[83] X. Li and G. B. McKenna, "Ultrathin polymer films: Rubbery stiffening, fragility, and t g reduction," *Macromolecules*, vol. 48, no. 17, pp. 6329–6336, 2015.

[84] A. Dwivedi *et al.*, "Mechanical response of polycarbonate with strength model fits," *DTIC Document*, 2012.

[85] A. M. Grande *et al.*, "Rate-dependent self-healing behavior of an ethylene-co-methacrylic acid ionomer under high-energy impact conditions," *Journal of Applied Polymer Science*, vol. 130, no. 3, pp. 1949–1958, 2013.

[86] K. L. Gordon *et al.*, "Ballistic puncture self-healing polymeric materials," NASA, Tech. Rep., 2017.

Supplementary Information for

SIZE MATTERS:

Impact Energy Absorption Across Five Decades of Length Scale

Jacob A. Rogers[a,*], Kailu Xaio[b], Paul T. Mead[a],

Charles U. Pittman[c], Jr., Justin W. Wilkerson[a], Edwin L. Thomas[b], Thomas E. Lacy, Jr.[a,**]

[a] Department of Mechanical Engineering, Texas A&M University, College Station, Texas, 77843.

[b] Department of Material Science and Engineering, Texas A&M University, College Station, Texas, 77843.

[c] Department of Chemistry, Mississippi State University, Starkville, Mississippi, 39762.

[*] Jacob A. Rogers, **Email:** jacob_rogers@tamu.edu

[**] Thomas E. Lacy, Jr., **Email:** telacyjr@tamu.edu

SI. Supplementary Information

SI.1. Polycarbonate Target Molecular Anisotropy Considerations

A polymer's unperturbed root-mean-square (RMS) end-to-end distance (R) is one measure for estimating its molecular size and is generally best determined through one or more experimental methods (*e.g.*, small-angle neutron scattering and/or small-angle X-ray scattering) [1, 2]. Theoretical models, however, can also approximate it by linking the polymer's physical properties to its dimensions. Flory [3] developed a widely used expression given by

$$R^2 = C_\infty N l_0^2, \tag{S1}$$

where C_∞ is the characteristic ratio, $N = M_w/m_0$ is the number of monomer units in the polymer chain, l_0 is the length of a single monomer, and m_0 is the average molecular weight per monomer. For polycarbonate (PC), $C_\infty \approx 2.4$, $l_0 \approx 7$ Å, and $m_0 \approx 127$ g/mol [4]. Taking $M_w \approx 56,000$ g/mol (Table S3), the approximate average number of monomer units is $N \approx M_w/m_0 = 56,000/127 = 441$. Therefore, an approximate RMS end-to-end distance for the PC used in this study is $R \approx 23$ nm, which indicates that the $h_t = 750$ nm (thinnest) film thickness was roughly 32 times (3,200%) larger than the PC RMS end-to-end distance.

The volume of the sphere which completely contains the PC chain (V) can be approximated from R as

$$V \approx \frac{4}{3}\pi \left(R^2\right)^{3/2}. \tag{S2}$$

Hence, the approximate volume taken up by a given PC molecule is $V \approx 51{,}000$ nm^3. The volume of PC target material beneath the projectile is $V_t = \pi/4\, d_p^2 h_t$ (Fig. 6d). For the same thickness sample, this target volume was roughly 1.0×10^5 times (1.0×10^7%) greater than the spherical volume containing the PC chain. These simple calculations suggest that *molecular* anisotropy is negligible and likely does not contribute to the observed changes in specific energy absorption or effective deformation area (*cf.* Fig. 9), even for the thinnest films.

SI.2. Polycarbonate Target Boundary Considerations

In-plane reflected waves from the target's boundary, influenced by the materials, shapes, and relative impact velocity of the projectile and target, can affect the dynamics of penetration and/or perforation. If the time taken for perforation (t_p) is significantly shorter than the duration for waves to travel from the impact point to the boundary and back (t_b), disruption from reflected waves is unlikely. Hence, evaluating the ratio t_p/t_b offers insight into potential boundary effects.

The time for a wave to travel to the boundary and back in a given target can be estimated as

$$t_b = 2\frac{r_b}{c_t}, \tag{S3}$$

where r_b is the in-plane radius from the impact point to the target boundary and $c_t = \sqrt{K_t/\rho_t}$, K_t, and ρ_t are the target's bulk sound speed, bulk modulus, and mass density, respectively. Similarly, the perforation/puncture time can be approximated as

$$t_p = \frac{2h_t}{v_i + v_r}, \tag{S4}$$

where h_t is the target film thickness, v_i is the projectile impact velocity, and v_r is the projectile residual velocity after impact. For the PC used in this study, K_t = 3,352 MPa and ρ_t = 1.2 g/cc. Hence, $c_t \approx$ 1,700 m/s for all samples. Using experimental v_i, v_r, and r_b measurements, values for t_b, t_p, and t_p/t_b were approximated for all PC samples (Table S1). These simple calculations show that for all scaled impacts, the perforation time was much less than the wave travel time ($t_p \lesssim 0.1t_b$), indicating reflected in-plane waves did not influence experimental perforation dynamics.

Table S1: Approximations of wave travel time (t_b), perforation time (t_p), and their ratio (t_p/t_b) for all PC samples. Calculated values are based on the target's bulk sound speed (c_t), projectile impact and residual velocities (v_i and v_r), and in-plane radius from the impact point to the boundary (r_b). The analysis shows that for all scaled impacts, the perforation time is significantly shorter than the wave travel time.

No.	d_p (μm)	v_i (m/s)	v_r (m/s)	t_p (ns)	r_b (mm)	t_b (ns)	t_p/t_b (%)
1	10,000	561	482	4,600	38	45,000	10
2	4,000	539	437	2,100	38	45,000	4.6
3	1,000	537	434	520	38	45,000	1.2
4	500	535	385	280	38	45,000	0.62
5	100	529	251	78	13	15,000	0.51
6	10	523	207	6.2	0.05	59	11
7	3	522	38	2.7	0.05	59	4.6

SI.3. Polycarbonate Target Material Properties

Comparative material studies require materials to be (at least) initially similar. Table S2 outlines the some key material properties for TUFFAK® (PC1) and RowTec® (PC2), including mass density, Rockwell hardness, tensile yield strength, tensile modulus, thermal conductivity, and coefficient of thermal expansion, as supplied by the manufacturers [5, 6]. Noteworthy is the minimal variation in properties between the two materials, confirming their comparability for the purposes of this investigation. This similarity is crucial, as it supports the assumption that any differences in the ballistic impact response of the materials can be attributed to the effects of length scaling effects rather than material inconsistencies/differences.

Table S2: Comparative material properties of TUFFAK® and RowTec® polycarbonates as provided by their manufacturers [5, 6].

Property	TUFFAK®	RowTec®	Difference (%)
Mass density (g/cc)	1.2	1.2	0%
Rockwell hardness (R scale)	R118	R118	0%
Tensile yield strength (MPa)	62	60	3%
Tensile modulus (GPa)	2.34	2.41	3%
Thermal conductivity (W/m/K)	0.19	0.19	0%
Coefficient of thermal expansion (1/K)	$68 \cdot 10^{-6}$	$68 \cdot 10^{-6}$	0%

SI.4. Gel Permeation Chromatography (GPC) Characterization of Polycarbonate Samples

Gel permeation chromatography (GPC) data was obtained for both commercial polycarbonate (PC) materials: PC1 (TUFFAK® from Plaskolite, LLC.) and PC2 (RowTec® from Rowland Advanced Polymer Films). Specifically, their molecular weight averages (M_n: number average, M_w: weight average, M_z: Z-average) and distribution (polydispersity $PDI = M_w/M_n$) were assessed using a TOSOH Ambient Temperature GPC instrument. The results for both materials were similar: M_n ranged from 27,737 to 28,927 g/mol, M_w around 55,800 g/mol, M_z approximately 87,800 g/mol, and PDI between 1.93 and 2.01 (Table S3). Figure S1a shows representative GPC chromatographs for PC1 and PC2 in millivolt (mV) *versus* log molecular weight [$\log(M)$] space, shedding light on molecular size distribution. Figure S1b shows cumulative weight percent versus molecular weight (M) normalized by the entanglement molecular weight $M_e \approx 2{,}500$ g/mol, indicating how molecular weight distribution correlates with the entanglement threshold. The comparable molecular weight distributions of the PCs confirm the materials' similarity, supporting their comparison across length scales.

SI.5. Target and Perforation Isotropy Inspection Using Cross Polarizers

Images of representative PC samples at each length scale were obtained using cross-polarizing optical microscopy (OM) to assess their uniformity and isotropy—especially crucial for ultra-thin samples [7]. The in-plane orientation of the targets was determined by analyzing camera pixel intensity values within a "pixel sampling region," identifying angles with the minimum ($\theta = 0°$) and maximum ($\theta = \pm 45°$) light transmission. This process was first applied to a representative as-received 2,380 μm thick sample (Fig. S3a and S3b), followed by an as-received 1,016 μm thick sample (Fig. S3c and S3d), an as-received 254 μm thick sample (Fig. S3e and S3f), an as-received 127 μm thick sample (Fig. S2a and S2b), a 30 μm thick compression-molded

Table S3: Gel permutation chromatography (GPC) results (M_n, M_w, M_z, and PDI) for the two commercial polycarbonate materials, PC1 and PC2 (see Supplementary Information, Sect. SI.4 and Fig. S1). The mass densities (ρ_t) and glass transition temperatures (T_g; obtained from DSC) of the target materials are also provided for reference.

Vendor/Material	M_n (g/mol)	M_w (g/mol)	M_z (g/mol)	PDI (M_w/M_n)	ρ_t (g/cc)	T_g (°C)
RowTec® (PC1)	27,737	55,711	87,908	2.01	1.20	149.2
TUFFAK® (PC2)	28,927	55,876	87,749	1.93	1.20	152.7

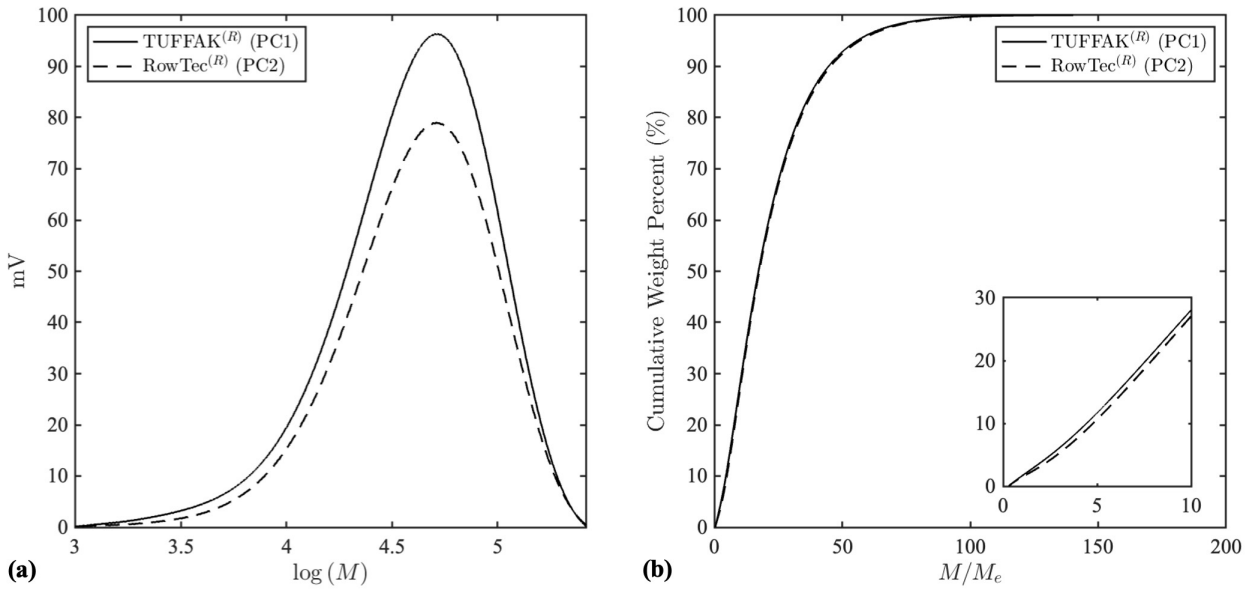

Figure S1: Gel permeation chromatography (GPC) analysis of polycarbonate (PC) samples PC1 and PC2: (a) a plot of detector response in millivolts (mV) *versus* the logarithm of molecular weight [$\log(M)$] and (b) cumulative weight percent of the PC as a function of molecular weight normalized by the entanglement molecular weight (M/M_e), with an inset showing the lower molecular weight range.

sample (Fig. S2c and S2d), and finally a spin-coated LIPIT sample (Fig. S2e and S2f). For the $h_t \approx 0.8$ μm and $h_t \approx 30$ μm films, the difference in light intensity at $\theta = 0°$ and $\theta = 45°$ was negligible (<1%). Hence, the spin-coating and compression-molding sample preparation processes did not induced significant material anisotropy. As the sample thickness increased ($h_t \approx 127$ μm and above; $h_t \gtrsim 160 h_t^{\mathrm{LIPIT}}$), the transmitted light intensity at $\theta = 45°$ did begin to increase. This is expected. Birefringence in thicker samples might not accurately reflect the material's inherent anisotropy. In thinner films that initially show no anisotropy, increasing thickness alone can lead to more interactions of polarized light with negligibly varying refractive indices and internal stresses, thereby amplifying birefringence effects. Material anisotropy in thicker films (if present) likely becomes less significant due to the averaging effect over the considerably larger thicknesses.

SI.6. Scaled Numerical Impact Simulations

The scaled h_t/d_p impact experiments were complemented with simulations using the Elastic Plastic Impact Computation (EPIC) code, which couples finite element analysis with smooth particle hydrodynamics to capture large-scale deformations, fracture, and fragmentation. Impact-induced equivalent plastic strain, strain rate, and temperature distributions, as well as specific energy absorption (E_p^*) and normalized deformation area (A_d/A_p), were computed for each length scale. In the simulations, the alumina projectiles were assumed to be perfectly rigid. The h_t thick PC targets were idealized and meshed in 3D quarter-symmetry using tetrahedral finite elements, where the characteristic element size increased with radial distance from

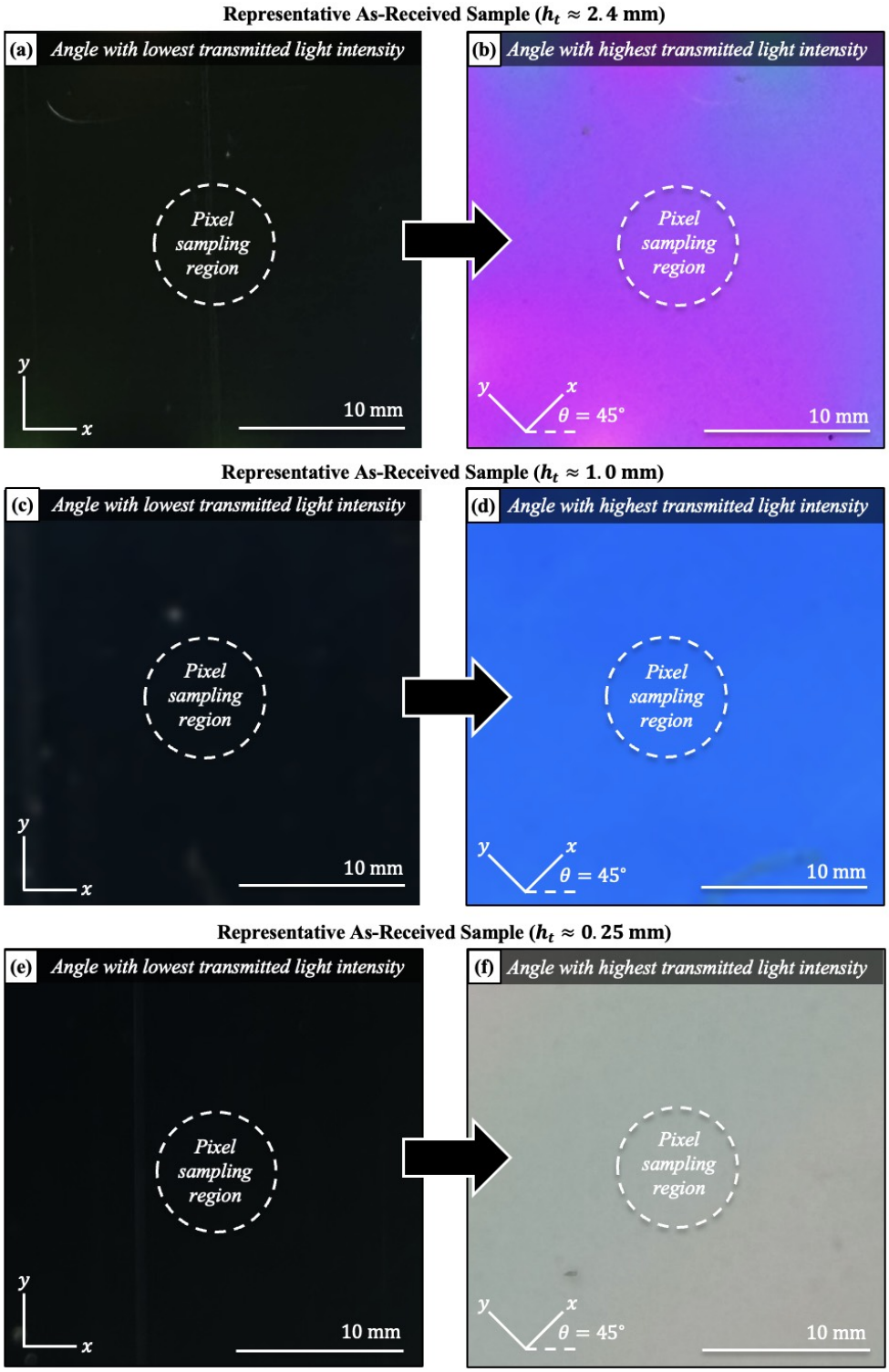

Figure S2: Cross polarizing optical microscopy images at in-plane angles $\theta = 0°$ (lowest light intensity) and $\theta = 45°$ (highest light intensity) for representative as-received (a, b) $h_t \approx 2.4$ mm, (c, d) $h_t \approx 1$ mm, and (e, f) $h_t \approx 0.25$ mm samples. Light intensity was sampled in a circular "pixel sampling region" to identify in-plane angle θ.

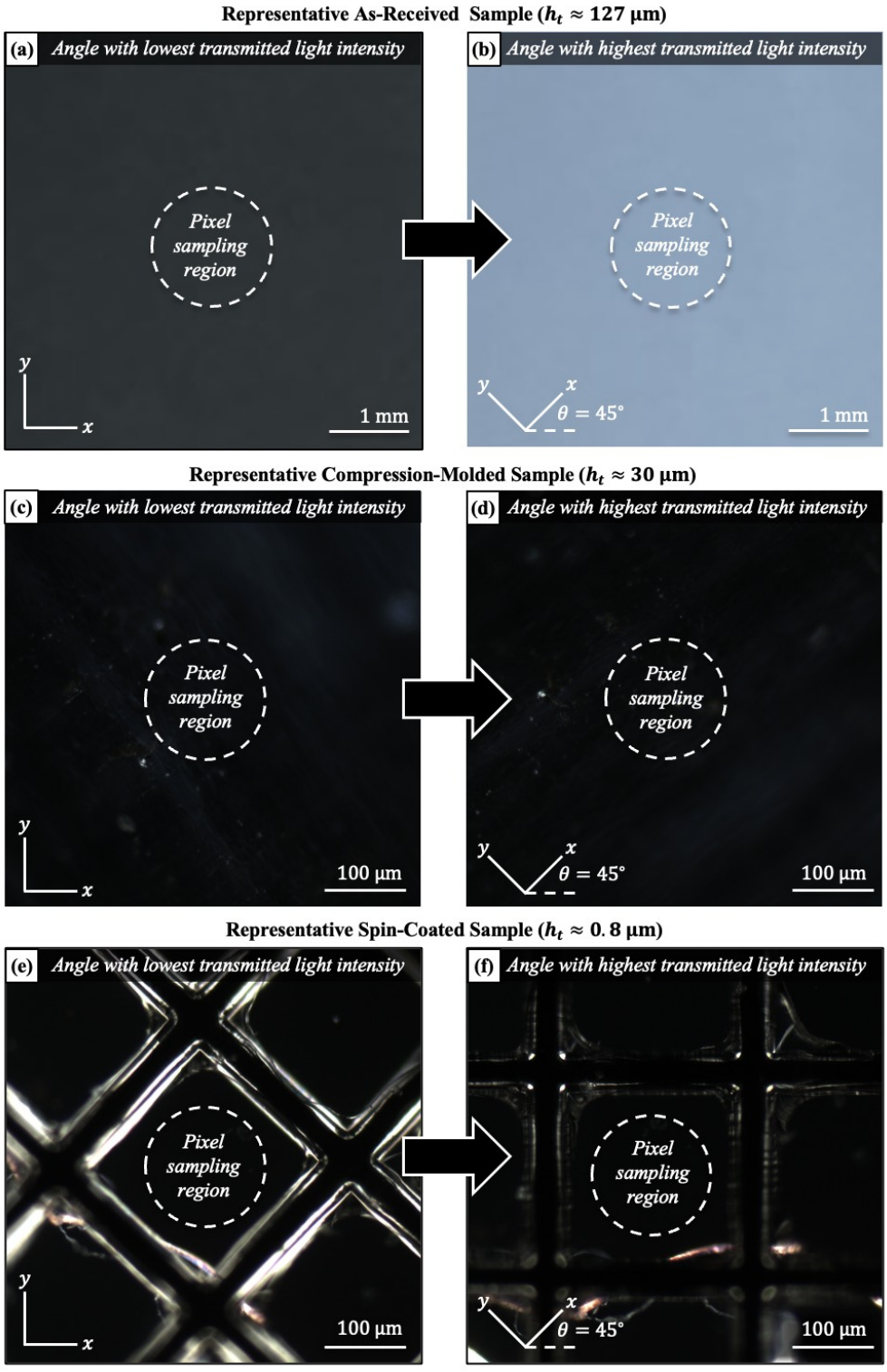

Figure S3: Cross polarizing optical microscopy images at in-plane angles $\theta = 0°$ (lowest light intensity) and $\theta = 45°$ (highest light intensity) for representative (a, b) as-received $h_t \approx 127$ µm, (c, d) compression molded, and (e, f) spin-coated samples. Light intensity was sampled in a circular "pixel sampling region" to identify in-plane angle θ.

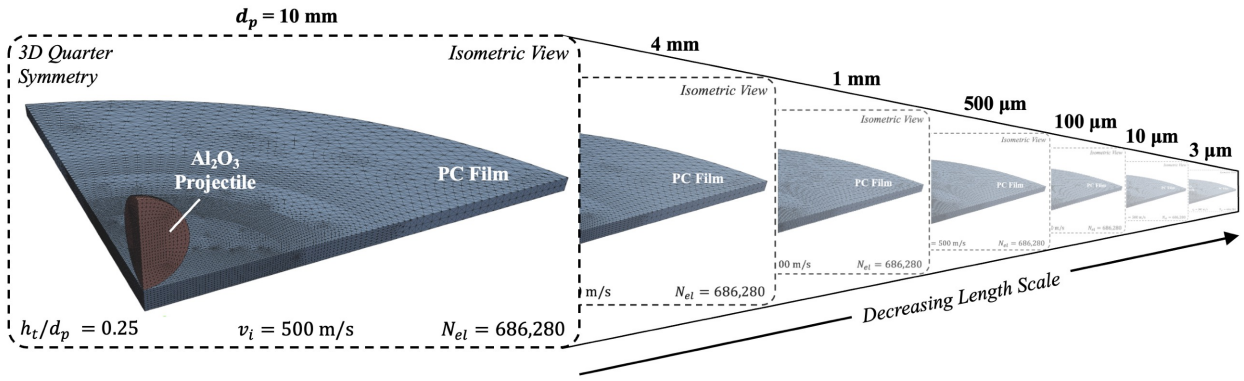

Figure S4: A straightforward illustration depicting the 3D quarter symmetric mesh (number of elements, N_{el} = constant = 686, 280) used for all EPIC code simulations along with the consistent impact conditions across the considered length scales ($h_t/d_p = 0.25$ and $v_i = 550$ m/s). Simulation time steps and run times varied, both decreasing with scale (*cf.* Table S4). The projectile diameter (d_p) is provided in bold to indicate the scale.

the axis of impact. Projectile and target meshes consisting of a combined total of $N_{el} = 686,280$ elements were utilized for all simulations, irrespective of scale; a mesh sensitivity analysis was performed to ensure a convergent solution. The finite element edge length for the projectile ($\sim 0.08 d_p$) matched that for the target in the projectile-target contact region. The element-to-particle conversion feature of the EPIC code was employed, with the equivalent plastic strain (ε_{eq}) required for conversion in the target set to 30%, a standard value for ductile materials [8]. In essence, these projectile and target meshes were linearly scaled such that the target thickness (h_t) matched that of the corresponding experiment (h_t/d_p = constant = 0.25; Fig. S4). Key simulation features, including time steps (Δt), run times (t_{run}), and number of elements (N_{el}), are summarized in Table S4.

The PC target material behavior was simulated using a Mie-Gruneisen EOS [9], JC constitutive model [10], and a JC fracture model [11]. A cubic form of the Mie-Gruneisen EOS was employed, *i.e.*,

$$P = (K_1\mu + K_2\mu^2 + K_3\mu^3)(1 - \Gamma\mu/2) + \Gamma E_s(1 + \mu), \tag{S5}$$

Table S4: A summary of the scaled impact simulations performed using the EPIC code. Key impact conditions, mesh geometry features, and simulation parameters are provided for reference.

No.	d_p (µm)	v_i (m/s)	h_t/d_p	Δt (ps)	t_{run} (µs)	N_{el}
1	10,000	550	0.25	2,070	80	686,280
2	4,000	550	0.25	831	35	686,280
3	1,000	550	0.25	208	9.2	686,280
4	500	550	0.25	104	4.4	686,280
5	100	550	0.25	19.2	0.65	686,280
6	10	550	0.25	2.08	0.30	686,280
7	3	550	0.25	0.62	0.15	686,280

d_p, projectile diameter; v_i, projectile impact velocity; h_t/d_p, target-thickness-projectile-diameter ratio; Δt, simulation time step; t_{run}, simulation run time; N_{el}, total number of elements.

Table S5: Mie-Gruneisen EOS [Eq. (S5)] and Johnson-Cook constitutive and fracture model [Eqs. (S6) and (S7)] parameters for the for PC target.

Parameter	**Value**	**Unit**
Yield stress, C_1	75.8	[MPa]
Hardening coefficient, C_2	68.9	[MPa]
Strain rate coefficient, C_3	0.52	-
Pressure coefficient, C_4	0.00	-
Hardening exponent, N	1.00	-
Softening exponent, m	1.85	-
Shear modulus, G	876	[MPa]
Strain to failure coefficient, D_1	0.00	-
Exponential coefficient, D_2	1.34	-
Stress triaxiality coefficient, D_3	-2.38	-
Strain rate coefficient, D_4	0.00	-
Temperature coefficient, D_5	0.00	-
Spall strength, σ_s	3.17	[GPa]
Bulk modulus, K_1	8.94	[GPa]
Quadratic M-G coefficient, K_2	4.56	[GPa]
Cubic M-G coefficient, K_3	43.5	[GPa]
Gruneisen coefficient, Γ	0.80	-
Melt temperature, T_m	533	K

where P is the pressure, K_1, K_2, and K_3 are polynomial coefficients, Γ is the Gruneisen coefficient, E_s is the internal energy per unit volume, and μ is given by the relationship $\mu = \rho/\rho_0$ - 1 where ρ is the current density and ρ_0 is the initial density. The JC constitutive model was used to determine the material's dynamic flow stress (σ),

$$\sigma = \left(C_1 + C_2\varepsilon_{eq}^N\right)\left(1 + C_3 \ln \dot{\varepsilon}_{eq}^*\right)\left[1 - (T^*)^m\right] + C_4 P, \tag{S6}$$

where C_1 is the uniaxial yield stress, C_2 is the hardening coefficient, ε_{eq} is the equivalent plastic strain, N is the hardening exponent, C_3 is the strain rate coefficient, $\dot{\varepsilon}_{eq}^*$ is the dimensionless total equivalent plastic strain rate (normalized by a strain rate of 1 s^{-1}), $T^* = (T - T_0)/(T_m - T_0)$ is the homologous temperature, T and T_0 are the current and reference temperatures, m is the softening exponent, C_4 is the pressure coefficient, and P is the hydrostatic pressure where compression has a positive sense. The equivalent plastic strain to fracture (ε_p^f) under constant conditions of $\dot{\varepsilon}_{eq}^*$ [*cf.* Eq. (S6)] is given by

$$\varepsilon_p^f = \left(D_1 + D_2 e^{D_3\sigma^*}\right)\left(1 + D_4 \ln \dot{\varepsilon}_{eq}^*\right)\left(1 + D_5 T^*\right), \tag{S7}$$

where D_1–D_5 are fitting parameters, $\sigma^* = \sigma_m/\sigma_{eq}$ is the pressure stress ratio (stress triaxiality [11]), σ_m is the mean normal stress, and σ_{eq} is the equivalent stress. In the simulations, material point "damage" is defined as the ratio of the accumulated equivalent plastic strain to fracture (*i.e.*, $\varepsilon_{eq}/\varepsilon_p^f$). An element or converted particle is considered to be fully damaged or fractured when this ratio reaches a value of unity. All material model and EOS parameters were sourced from the EPIC materials library or the literature [12]. These values, as well as other important target material parameters, are reported in Table S5.

SI.7. Simulation Considerations for Scaled Impacts

Length-scaled impact simulations necessitate careful consideration of material properties, features, and behaviors that are often negligible at the macroscale. These include material surface effects (adhesion, friction, surface tension), microstructure and morphology, defects and imperfections, as well as potentially drastic changes in phase, adiabatic heating, deformation, failure, and more. The mechanical behavior of polymers is highly sensitive to temperature, pressure, and testing rate. Since impact experiments induce extreme conditions with dynamic gradients in temperature, strain, strain rate, and stress state that evolve spatially and temporally, ballistic deformation of polymers is particularly susceptible to length scale effects. In addition, the surface-to-volume ratio is much higher at the microscale, meaning surface effects, including surface tension and surface energy, can potentially compete with or dominate over bulk properties [13, 14]. While macroscale properties assume an averaged, isotropic orientation of molecules, microscale properties can be highly anisotropic due to alignment of polymer chains arising from processing or geometric constraints (*e.g.*, target thickness). The influence of polymer microstructural features, such as chain ends, entanglements, and voids, can have an amplified effect on local mechanical properties, such as impact resistance and ductility [15, 16]. Polymers may experience different phase transitions at the microscale due to constraints on molecular movement and phase separation processes [17, 18]. The microscale thermal conductivity of polymers can deviate from their bulk properties. This conductivity is heavily influenced by the microstructure, where features such as chain structure, crystallinity, crystal form, and the orientation of polymer chains in thin films play a more crucial role than the material's density [19]. Such features cannot be rendered using macroscale continuum approaches. Moreover, due to the relative length scale and irregular nature of these polymer features, multi-scale continuum-based codes are likely also inadequate.

As deformation rates increase with decreasing scale, thermoplastics can exhibit significantly different viscoelastic and fracture behaviors compared to bulk materials due to a competition between loading rate and rate of polymer chain motion/alignment and entanglement dynamics. Furthermore, the validity of using conventional (bulk) material parameters at ultra-high strain rates exceeding 10^4 s^{-1} is questionable due to the current inability of reliably quantifying material properties at such rates. Material features and local variations in material properties that are negligible or "averaged out" at macroscales (*i.e.*, continuum or bulk material properties) can become unavoidably magnified at the microscale. Yet, it is macroscale material properties that are used to model material elasticity, plasticity, thermal conductivity, fracture, failure, and more. Hence, the failure of continuum-based Finite Element Analysis (FEA) and/or Smooth Particle Hydrodynamics (SPH) computation to accurately simulate microscale impact behavior is not surprising. Since the issues reside with the continuum-based assumptions, they are not unique to EPIC and likely exist for other continuum codes, including LS-DYNA [20], Ansys Autodyn [21], CTH [22], and ALE3D [23].

Coarse-graining molecular dynamics (MD) might offer a more precise representation of microscale behaviors [24].

The EPIC simulations were analyzed more thoroughly to display these considerations given only changes in the impact scenario's length scale ($v_i \equiv 550$ m/s and $h_t/d_p \equiv 0.25$). This inspection is also critical to identifying potential areas of improvement for future modeling. One simple approach involves capturing target cross-sectional snapshots depicting elemental ε_{eq}, $\dot{\varepsilon}_{eq}$, and T values at a certain time t post-impact, such as at $t = 0.5t_p$ [where $t_p \approx 2h_t/(v_i+v_r)$], when the projectile is roughly midway through perforation. At this stage, significant deformation is observable for all scaled impacts without the onset of extensive material failure. Such snapshots were obtained for particles with $d_p = 10{,}000$ μm (Figs. S5a–S5c), $d_p = 4{,}000$ μm (Figs. S5d–S5f), $d_p = 1{,}000$ μm (Figs. S5g–S5i), $d_p = 500$ μm (Figs. S5j–S5k), $d_p = 100$ μm (Figs. S5m–S5o), $d_p = 10$ μm (Figs. S5p–S5r), and $d_p = 3$ μm (Figs. S5s–S5u) simulated impact perforations. These PC target cross sections are arranged in decreasing order of d_p, with each column representing a different variable: (left to right) ε_{eq}, $\dot{\varepsilon}_{eq}$, and T. In each snapshot, the rigid alumina projectile has been hidden for ease of visualization. The simulation time after impact (t) and length scale are indicated in the bottom left and right, respectively. The color bars at the bottom of each column correlate the colors used in the plots with their quantitative values. Variations in the deformation geometry are minor: the instantaneous "crater" size, penetration depth, and back-face bulging seem to be similar regardless of the scale. As d_p decreases, the elements possessing peak ε_{eq} values (*i.e.*, the element-to-particle conversion strain of 30%) appear to shift outward symmetrically from directly beneath the projectile to lateral locations. The number of elements with $\varepsilon_{eq} \approx 0.3$ also seem to decrease. Reducing the length scale leads to a rise in peak calculated strain rates (up to $\dot{\varepsilon}_{eq} \sim 10^{10}$ s^{-1}), without significantly affecting the overall distribution. Interestingly, the predicted temperature distribution remains largely unchanged, with peak temperatures reaching just $T \approx 0.75T_m$ for the $d_p = 3$ μm impact.

In essence, the EPIC simulations fail to accurately mirror the physics seen in the impact experiments, as they show little variation in strain, strain rate, and temperature, as well as overall deformation and energy absorption, with decreasing length scale. This largely invariant response not only disagrees with experimental observations but also is contrary to expectations that *nominal* (not just peak) strain and heating rates should rise notably with decreasing scale due to shorter perforation times. Moreover, despite a significant increase in predicted *peak* strain rates (from 10^6 s^{-1} to 10^{10} s^{-1}), the lack of noticeable changes in the simulation outcomes suggests that the material models do not capture changes in material strain and strain rate hardening, thermal softening, melting, *etc.* These clear discrepancies underline the need to develop or rethink material models to better capture the behaviors observed in scaled impacts. This study, of course, is limited to a single material, PC, which is homogeneous and amorphous at all examined scales. Introducing

hierarchical material inhomogeneity and anisotropy, that are present in metals and carbon nanotube mats, into computational models would substantially increase their complexity. The simulation results included in this study simply demonstrate modeling limitations and potential areas for advancements.

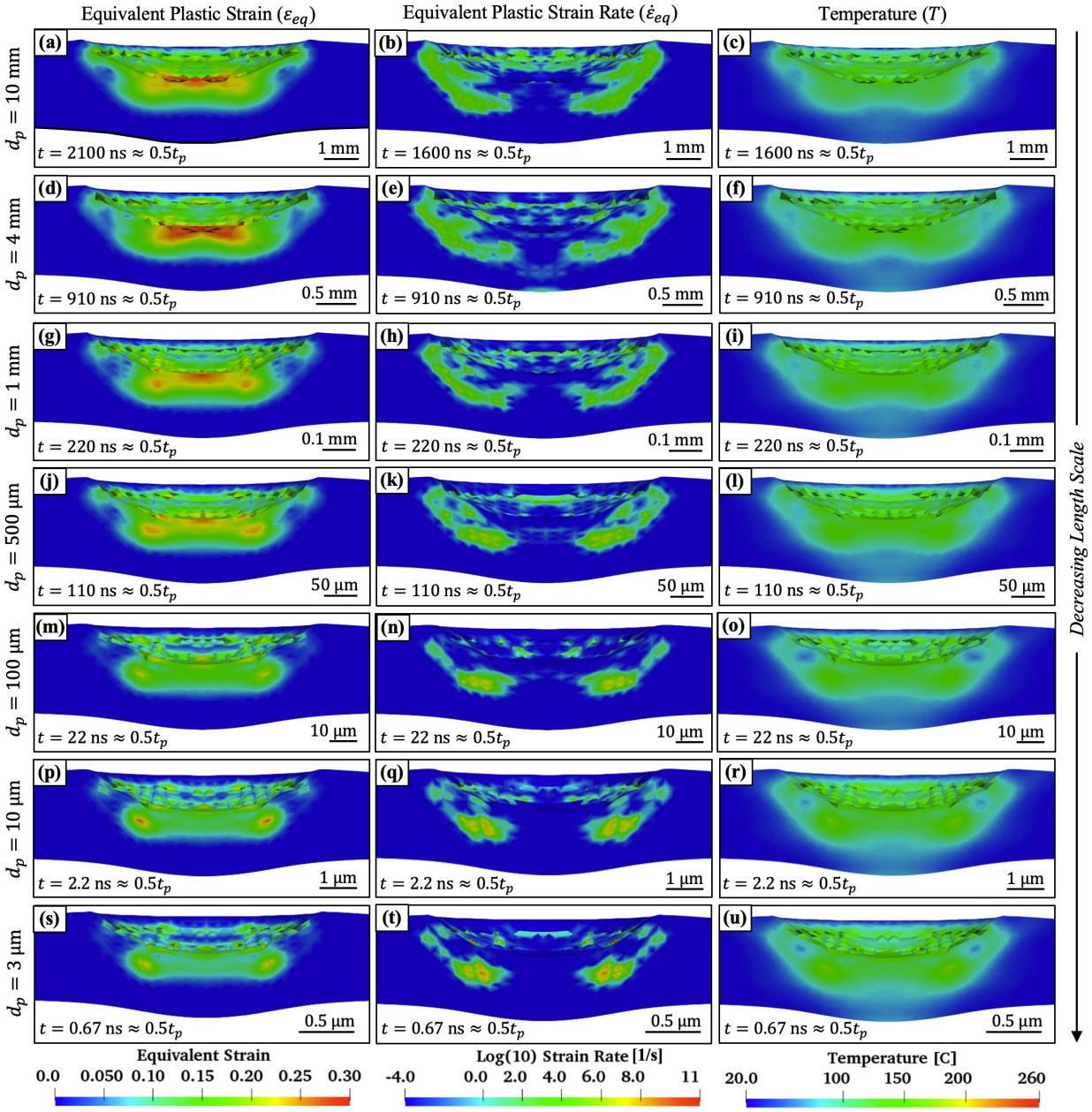

Figure S5: Cross-sectional EPIC simulation snapshots for the (a–c) d_p = 10 mm, (d–f) d_p = 4 mm, (g–i) d_p = 1 mm, (j–l) d_p = 500 µm, (m–o) d_p = 100 µm, (p–r) d_p = 10 µm, and (s–u) d_p = 3 µm. Each column in the image array corresponds to a different spatially vary parameter: (a, d, g, j, m, p, s) equivalent plastic strain (ε_{eq}), (b, e, h, k, n, q, t) equivalent plastic strain rate ($\dot{\varepsilon}_{eq}$), and (c, f, i, l, o, r, u) temperature (T). The time after impact ($t \approx 0.5t_p \approx 0.5\,{}^{h_t}/_{v_i}$) is provided in the bottom right corner of each snapshot.

References for Supplementary Material

[1] L. Feigin, D. I. Svergun, *et al.*, *Structure analysis by small-angle X-ray and neutron scattering*. Springer, 1987, vol. 1.

[2] C. M. Jeffries *et al.*, "Small-angle x-ray and neutron scattering," *Nature Reviews Methods Primers*, vol. 1, no. 1, p. 70, 2021.

[3] P. J. Flory and M Volkenstein, *Statistical mechanics of chain molecules*, 1969.

[4] L. Fetters *et al.*, "Connection between polymer molecular weight, density, chain dimensions, and melt viscoelastic properties," *Macromolecules*, vol. 27, no. 17, pp. 4639–4647, 1994.

[5] *Rowtec® pc1 graphic arts polycarbonate film*, 2023, p. 2. [Online]. Available: `https://www.orafol.com/fileadmin/americas/images/literature/rowland_apf_-_tables/rowtec/rowtec-pc1_table.pdf`.

[6] *Tuffak® gp polycarbonate sheet*, 2022, p. 2. [Online]. Available: `https://plaskolite.com/docs/default-source/tuffak-assets/product-data-sheets/pds004_gp.pdf`.

[7] I. J. Hodgkinson and H. W. Qi, *Birefringent thin films and polarizing elements*. World Scientific, 1998.

[8] G. R. Johnson *et al.*, "An algorithm to automatically convert distorted finite elements into meshless particles during dynamic deformation," *International Journal of Impact Engineering*, vol. 27, no. 10, pp. 997–1013, 2002.

[9] E. Grüneisen, "Theorie des festen zustandes einatomiger elemente," *Annalen der Physik*, vol. 344, no. 12, pp. 257–306, 1912.

[10] G. R. Johnson, "A constitutive model and data for materials subjected to large strains, high strain rates, and high temperatures," *Proc. 7th Inf. Sympo. Ballistics*, pp. 541–547, 1983.

[11] G. R. Johnson and W. H. Cook, "Fracture characteristics of three metals subjected to various strains, strain rates, temperatures and pressures," *Engineering fracture mechanics*, vol. 21, no. 1, pp. 31–48, 1985.

[12] A. Dwivedi *et al.*, "Mechanical response of polycarbonate with strength model fits," *DTIC Document*, 2012.

[13] P. A. O'Connell and G. B. McKenna, "The stiffening of ultrathin polymer films in the rubbery regime: The relative contributions of membrane stress and surface tension," *Journal of Polymer Science Part B: Polymer Physics*, vol. 47, no. 24, pp. 2441–2448, 2009.

[14] S. Xu *et al.*, "Unusual elastic behavior of ultrathin polymer films: Confinement-induced/molecular stiffening and surface tension effects," *The Journal of Chemical Physics*, vol. 132, no. 18, 2010.

[15] N. R. Velez *et al.*, "Extreme ductility in freestanding polystyrene thin films," *Macromolecules*, vol. 53, no. 19, pp. 8650–8662, 2020.

[16] J.-H. Lee *et al.*, "Effect of confinement on stiffness and fracture of thin amorphous polymer films," *ACS Macro Letters*, vol. 1, no. 1, pp. 122–126, 2012.

[17] J. M. Torres *et al.*, "Elastic modulus of amorphous polymer thin films: Relationship to the glass transition temperature," *Acs Nano*, vol. 3, no. 9, pp. 2677–2685, 2009.

[18] O. K. Tsui and H. Zhang, "Effects of chain ends and chain entanglement on the glass transition temperature of polymer thin films," *Macromolecules*, vol. 34, no. 26, pp. 9139–9142, 2001.

[19] H. Chen *et al.*, "Thermal conductivity of polymer-based composites: Fundamentals and applications," *Progress in Polymer Science*, vol. 59, pp. 41–85, 2016.

[20] *Ls-dyna*, `https://lsdyna.ansys.com/`, Accessed: [your date of access].

[21] *Ansys autodyn*, `https://www.ansys.com/products/structures/ansys-autodyn`, Accessed: [your date of access].

[22] *Cth*, `https://www.sandia.gov/cth/`, Accessed: [your date of access].

[23] *Ale3d*, `https://ale3d4i.llnl.gov/`, Accessed: [your date of access].

[24] S. Y. Joshi and S. A. Deshmukh, "A review of advancements in coarse-grained molecular dynamics simulations," *Molecular Simulation*, vol. 47, no. 10-11, pp. 786–803, 2021.